Polarimetric Interferometry and Differential Interferometry

Martin Hellmann[1], Shane R. Cloude[2]

[1]German Aerospace Center (DLR), Strategy and Networking, Linder Höhe, 51140 Köln, Germany
E-mail: martin.hellmann@dlr.de

[2]School of Electrical and Electronic Engineering University of Adelaide South Australia 5005
Tel/Fax : +61 (0)8 8303 8313/4360 web:http://www.eleceng.adelaide.edu.au/Personal/scloude/

Abstract

This Lecture mainly based on [1, 2] presents the role of Polarimetry in SAR Interferometry. A general formulation for vector wave interferometry is presented that includes conventional scalar interferometry presented in the respective former lecture as a special case. Based on this formulation, the coherence optimization problem can be solved to obtain the optimum scattering mechanisms that lead to the best phase estimates. Comparison with conventional single-polarization estimates illustrates the significant processing gains that are possible if there is access to full polarimetric interferometric data. A comparison with conventional single-polarization presented in former lectures illustrates the significant processing gains that are possible if access to full polarimetric interferometric data is possible. The strong polarization depends of the coherence will be addressed and the analytical solution for optimum polarization states that maximize the interferometric coherence will be derived and applied to experimental data. These improved interferogrammes allow an improvement of the accuracy of derived DEM products.

The introduction of a new coherent decomposition theorem for interferometric applications based on the Singular value spectrum of a 3 x 3 complex matrix allows the decomposition of polarimetric interferometric problems into a set of coherent scattering mechanisms. As a consequence, it is possible to generate interferograms related to certain independent scattering mechanisms and extract the height differences between them. The limitation of this technique is the existence of independent scattering mechanisms located at different height positions.

To explain the physical origin of these mechanisms, a coherent electromagnetic scattering model will be established which, additionally, can be used to establish the suitability of the decomposition algorithm for solving the problem of estimating the location of the effective scattering center, which is a critical point in the physical interpretation of interferograms. However, these introduction of Polarimetry in interferometric processing requires that fully coherent polarimetric data must be collected in order to separate the scattering mechanisms.. In this connection polarimetric Differential Interferometry will be considered also.

The phase difference between the optimum interferograms obtained by the application of the algorithm on the SIR-C data turned out to be strongly correlated with the actual forest height. This was a major result indicating the potential of the coherent combination of polarimetry and interferometry.

[1] Cloude, S.R."Polarimetric SAR Interferometry", IEEE Trans.GRS. vol. 36. no. 5. September 1998
[2] Cloude S.R, and K.P. Papathanassiou. "Polarimetric SAR Interferometry." *IEEE Trans. Geosci. Rem. Sens.*, vol. 36, no. 5, pp. 1551-1565, September 1998.

1. Introduction

Polarimetric SAR Interferometry was a first step in the abatement of the scattering ambiguity problem in the height direction. By combining interferometric and polarimetric techniques, it enables the separation of different scattering mechanisms within a resolution cell and at the same time, the estimation of the associated heights. Both, radar polarimetry and radar interferometry are phase sensitive techniques. The use of polarimetric SAR data has been widely addressed in the last decade. The tight relation between natural media physical properties and their polarimetric features leads to highly descriptive results that can be interpreted by analyzing underlying scattering mechanisms. Interferometric data on the other hand provide information concerning the coherence of the scattering mechanisms and can be used to retrieve observed media structures and complexity. The complementary aspect of polarimetric and interferometric information leads to a combination of both approaches. In 'Polarimetric-Interferometric Synthetic Aperture Radar (POL-INSAR) Imaging' it is possible to recover textural and

spatial properties simultaneously. This includes the extraction of 'Digital Elevation Maps (DEM)' from either 'fully Polarimetric (scattering matrix) or interferometric SAR image data takes' with the additional benefit of obtaining co-registered three-dimensional 'POL-IN-DEM' information.

Over the next few years several free-flying remote sensing satellites will be deployed in orbit, providing the international scientific, commercial and military communities with a wealth of new data. Many of these will carry advanced multi-channel imaging radars designed to combine various levels of polarisation diversity with radar interferometry.

Polarimetric interferometry has proved to be a valuable tool for many applications. One is remote sensing where it has been shown in several recent publications that by using interferograms in multiple polarisation channels, estimation of vegetation height, underlying ground topography and mean extinction is possible [11,14,23].

Polarimetric Synthetic Aperture Radar interferometry (POLInSAR) can also be used to enhance the detection of military targets hidden beneath foliage. The key idea is to note that for random volume scattering the interferometric coherence is invariant to changes in wave polarisation. On the other hand, in the presence of a target the coherence changes with polarisation. It can be shown that under general symmetry constraints this change is linear in the complex coherence plane. These observations can be used to devise a filter to suppress the returns from foliage clutter while maintaining the signal from hidden targets.

2. Radar Polarimetry

As shown in a previous lecture, an important extension to single-channel SAR remote sensing is the utilisation of polarised waves. A polarimetric SAR system measures the electric field, backscattered by the scene, including its polarisation state. The interaction of the transmitted wave with a scattering object transforms its polarisation.

One special characteristic of SAR polarimetry is that it allows a discrimination of different types of scattering mechanisms. This becomes possible because the observed polarimetric signatures depend strongly on the actual scattering process. In comparison to conventional single-channel SAR, the inclusion of SAR polarimetry consequently can lead to a significant improvement in the quality of data analysis. Certain polarimetric scattering models even provide a direct physical interpretation of the scattering process, allowing an estimation of physical ground parameters like soil moisture and surface roughness [11], as well as unsupervised classification methods with automatic identification of different scatterer characteristics and target types [4,5].

SAR polarimetry additionally offers some limited capability for separating multiple scattering mechanisms occurring inside the same resolution cell and can be deemed as a first step in resolving the ambiguous scattering problem in SAR, as mentioned above. With polarimetric decomposition techniques a received signal can be split into a sum of three scattering contributions with orthogonal polarimetric signatures. This can be used for extracting the corresponding target types in the image, even in the case that they are occurring superimposed. Also, if a signal is disturbed by undesired orthogonal contributions, in this way the relevant components can be extracted.

3. The Phase

In radar polarimetry [1] we analyze the shape of the transmit (and receive) polarisation ellipse, as shown schematically in Figure 1a, for the purposes of improved information extraction. Figure 1a shows the spatial helix resulting from a combination of horizontal (H, in green) and vertical (V, in blue) transmitted components.
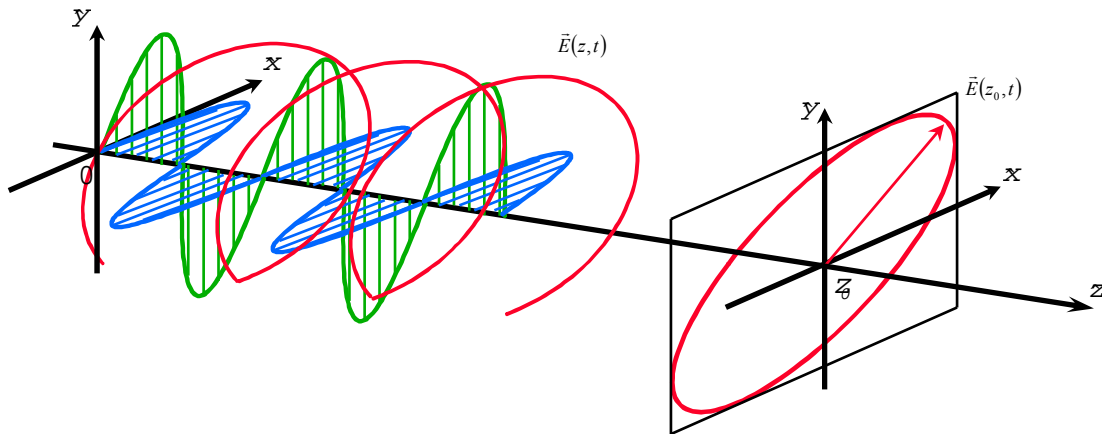
Figure 1a : The Polarisation Ellipse and Spatial helix decomposed into orthogonal components x (horizontal H) and y (vertical V) [Pottier, lectures on polarimetry]

By controlling the relative amplitudes we can rotate the polarisation from H through 45 degrees to V. However, by adjusting the relative timing (phase) of the blue and green components we can also adjust the shape of the ellipse as shown in Figure 1b. It is this combined amplitude and phase dimension that leads to increased information content in remote sensing applications, since the level of scattering we observe from natural terrain depends on the shape of this ellipse. [1,2,3,4,5]
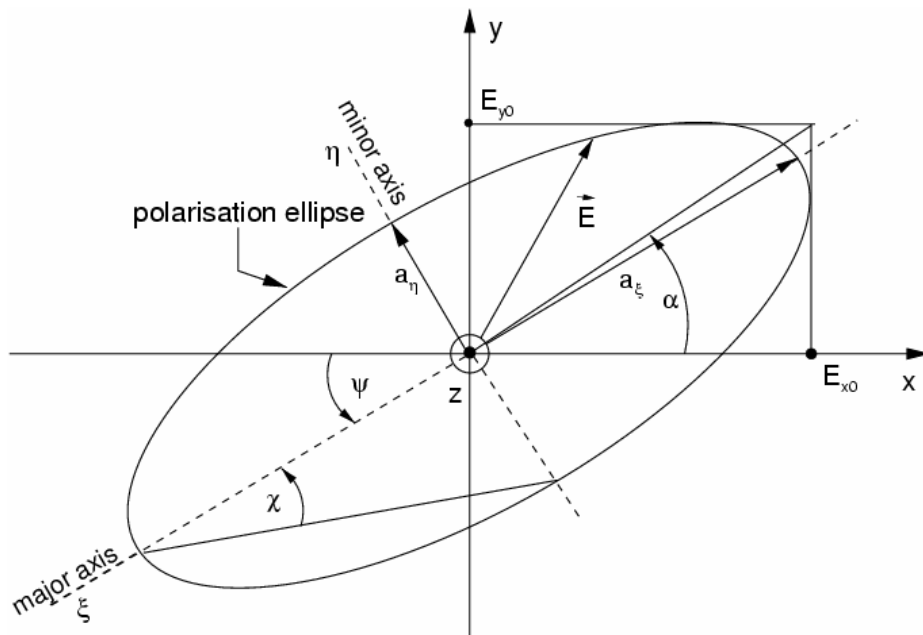

Figure 1b : The Polarisation Ellipse

To represent this combined amplitude and phase control mathematically, we describe the wave using a pair of complex numbers, e_x and e_y as shown in equation 1. The phase difference i.e. $\varphi = \arg(e_x e_y*)$ then controls the shape of the ellipse, with linear polarisations defined by $\varphi = 0$. Note that the ellipse is actually a dynamic quantity, being the time locus of the helix in a fixed spatial plane. Consequently the locus can move clockwise or counter-clockwise (when viewed in the −z direction), corresponding to what are termed left and right-handed polarisations respectively. The set of all possible left and right handed ellipses can then be conveniently mapped onto the northern and southern hemispheres of the Poincaré sphere. Figure 1c [1,6]
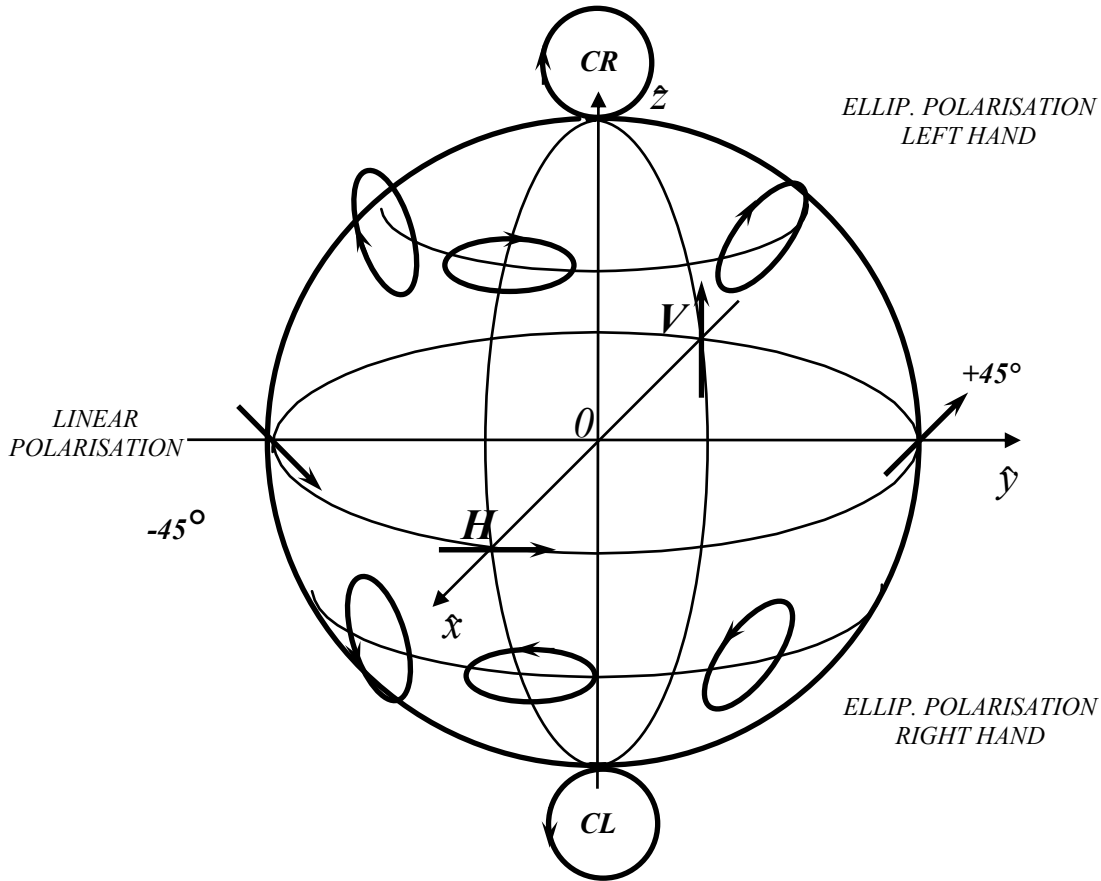
Figure 1c : The Poincaré sphere

Furthermore, our ability to extract quantitative information rests on the stability of this phase or the robustness of the spatial helix to small time and spatial shifts. A generic way to define the stability of this helix is to use the wave coherency matrix [J], taken at a point in space with position vector r. and formed as an average of all possible complex products between e_x and e_y as shown in equation 1, [6]

$$ e_x \hat{x} + e_y \hat{y} \Rightarrow \underline{E} = \begin{bmatrix} e_x \\ e_y \end{bmatrix} \Rightarrow [J] = \left\langle \underline{E}.\underline{E}^{*T} \right\rangle = \begin{bmatrix} \left\langle e_x(\underline{r})e_x^*(\underline{r}) \right\rangle & \left\langle e_x(\underline{r})e_y^*(\underline{r}) \right\rangle \\ \left\langle e_y(\underline{r})e_x^*(\underline{r}) \right\rangle & \left\langle e_y(\underline{r})e_y^*(\underline{r}) \right\rangle \end{bmatrix} $$

(1)

As its name suggests, this matrix allows us to calculate not only the wave intensity (from the diagonal components) but also the coherence, which is a measure of the phase stability of the wave, as defined in equation 2 [7].

$$ \tilde{\gamma}_{xy} = \frac{\left\langle e_x(\underline{r})e_y^*(\underline{r}) \right\rangle}{\sqrt{\left\langle e_x(\underline{r})e_x^*(\underline{r}) \right\rangle . \left\langle e_y(\underline{r})e_y^*(\underline{r}) \right\rangle}}, 0 \le \left| \tilde{\gamma}_{xy} \right| \le 1 $$

(2)

A key benefit of employing ratios such as equation 2 is that absolute amplitude terms cancel, so removing some of the structural dependence in scattering from random media. It is this observation that shifts interest in polarimetry towards the study of ratios as potentially more robust indicators of physical structure (see examples in table I).

In active microwave sensing we assume $\left|\widetilde{\gamma}_{xy}\right|=1$ for the transmitted wave and hence the transmitted spatial helix is very stable. However, when the wave is scattered or reflected from natural media, its phase and amplitude will in general be modified (as shown schematically in Figure 2a). This process again must be described by a set of complex numbers, this time by a set of four, being the elements of the coherent scattering matrix [S] defined as shown in equation 3. This matrix characterises all possible phase and amplitude changes due to copolar (diagonal elements) and cross-polar (off diagonal) scattering. In practice, for the common case of backscatter, the reciprocity theorem for electromagnetic waves reduces this set to three complex numbers, as the cross-polarisation terms are equal $S_{HV} = S_{VH}$. Note that while this is widely true, there are a few special but important cases where it breaks down, as for example in low frequency radio wave propagation through the ionosphere, where the earths magnetic field lines break this reciprocity symmetry and as a result the cross polarisation terms are no longer equal. This observation can be used to calibrate the effects of Faraday rotation due to trans-ionospheric propagation, an important issue for the deployment of low frequency space-borne radars [8].

$$\underline{E}_s = \frac{e^{ikr}}{r}[S].\underline{E} \Rightarrow [S] = \begin{bmatrix} S_{HH} & S_{HV} \\ S_{VH} & S_{VV} \end{bmatrix} \xrightarrow[S_{HV}=S_{VH}]{reciprocity} \underline{k} = \begin{vmatrix} S_{HH} \\ \sqrt{2}S_{HV} \\ S_{VV} \end{vmatrix} \Rightarrow [C] = \left\langle \underline{k}.\underline{k}^{*T} \right\rangle$$

(3)

One key idea in polarimetry is that if we know all four of these [S] matrix elements then we can calculate the phase stability of the scattered signal for arbitrary incident ellipse, using a 3 x3 covariance matrix [C] as shown in equation 3. In this way we don't have to actually change the shape of the transmit ellipse (which would call for control of the antenna and microwave electronics) but can simulate the same effect off-line in the processing stages. For this reason there has been a lot of interest in the development of microwave switching systems that are capable of measuring all four elements of [S] (the simplest is to switch each transmit pulse between X and Y orthogonal polarisations with simultaneous reception of the X and Y components). Note that one important step is to calibrate system distortion effects due to crosstalk (which causes problems with estimation of the off-diagonal elements of [S]) and channel imbalance due to phase and amplitude distortions of the radar system itself. The development of robust calibration procedures has been a key enabling step in the quantitative exploitation of this technology [9]. Such systems are called 'quadpol' as they measure 4 complex numbers for each pixel in the image and allow the user to explore the whole Poincaré sphere. There are currently several mature airborne quadpol radar sensors with such a capability, but significantly there will soon be a new generation of free-flying satellite radars operating in this mode. The European Terrasar-X/L, Japanese ALOS-PALSAR and Canadian Radarsat-2 are important examples. The main question then becomes, how can we find the best polarisation combination to derive information products exploiting the scattering of waves from surfaces and vegetation? To answer this we must look more carefully at equation 2 and the whole issue of coherence.

4. Coherence and Entropy

To calculate polarimetric coherence, we first choose a pair of polarisations x and y, then measure the (complex) components of the signal in these two channels and estimate the coherence by averaging. However, even for a fixed wave, the coherence obtained with this method will depend on the choice of our reference pair x and y (e.g. choosing x=y will give a coherence of 1, while less obvious but more important is the idea that for every wave we can choose an orthogonal pair x and y so that the coherence is zero). This goes against the idea that the spatial helix is somehow independent of the co-

ordinates we use to represent it, and that consequently we should be able to describe its stability in co-ordinate invariant terms. One way to do this is to describe the helix stability using a generalised coherence or entropy (another popular way is to use the degree of polarisation [6]). The wave entropy is formally defined from the ratio of eigenvalues of [J] (see equation 4) and has a value of 0 when the helix is perfectly stable and 1 when it becomes noise like [2,4,6].

$$0 \leq H_w = -\sum_{i=1}^{2} p_i \log_2 p_i \leq 1, \quad p_i = \frac{\lambda_i([J])}{\sum \lambda} \tag{4}$$

By extension, we can also describe the loss of helix stability after scattering by the entropy of the 3 x3 covariance matrix [C] in equation 3, as defined in equation 5 [2,4]

$$0 \leq H_s = -\sum_{i=1}^{3} p_i \log_3 p_i \leq 1, \quad p_i = \frac{\lambda_i([C])}{\sum \lambda} \tag{5}$$

It is important to realize that this scattering entropy is characteristic of the scattering medium itself. For example, for low frequency volume scattering from a cloud of ellipsoidal particles of dielectric constant ε_r and axial ratio m, the normalized eigenvalues of [C] can be evaluated explicitly as shown in equation 6 [2,4,16,17]

$$m = \begin{cases} >1 & \text{prolate particles} \\ 1 & \text{spherical particles} \\ <1 & \text{oblate particles} \end{cases} \Rightarrow R = \frac{m\varepsilon_r + 2}{m + \varepsilon_r + 1} \Rightarrow \begin{cases} \lambda_1 = 2R^2 + 6R + 7 \\ \lambda_2 = (R-1)^2 \\ \lambda_3 = (R-1)^2 \end{cases} \tag{6}$$

For spherical particles (R =1) this leads to zero entropy but for a cloud of 'wet dipoles' (m and ε_r large) the entropy rises to 0.95. Hence a measurement of entropy relates to information about composition of the volume. Importantly, we can estimate scattering entropy numerically on a pixel-by-pixel basis from quadpol radar imaging data. Figure 2b shows an example of the entropy or phase stability of a mixed scene, being the Oberpfaffenhofen area as collected by the DLR L-Band ESAR system. We note that over non-vegetated surfaces (left bottom corner in figure 2b) the entropy is low and hence the scattered wave helix is very stable for all types of transmit polarisation. This can be exploited for quantitative moisture and roughness estimation of non-vegetated land surfaces by choosing appropriate robust ratios of scattering elements as shown for example in table I. [10,11,12,13,14,15]

The urban areas (upper right corner) in figure 2 show moderate entropy, but the worst case arises for vegetation (lower right corner). Here we see high entropy due to volume scattering by the random components of the vegetation cover (as in equation 6). These observations are independent of the actual scene considered and hence have been suggested by several authors as suitable for robust unsupervised classification of land cover [3,4,5,13].

While useful for classification and limited composition studies, such high entropy for vegetation cover restricts our ability to fully exploit polarisation for quantitative parameter estimation. Yet vegetation cover is of prime importance in remote sensing applications. Somehow, in order to proceed, we have to find a way to reduce the entropy. Importantly this can be achieved by combining polarimetry with interferometry, to form the new topic of imaging polarimetric interferometry or POLInSAR as we now show.
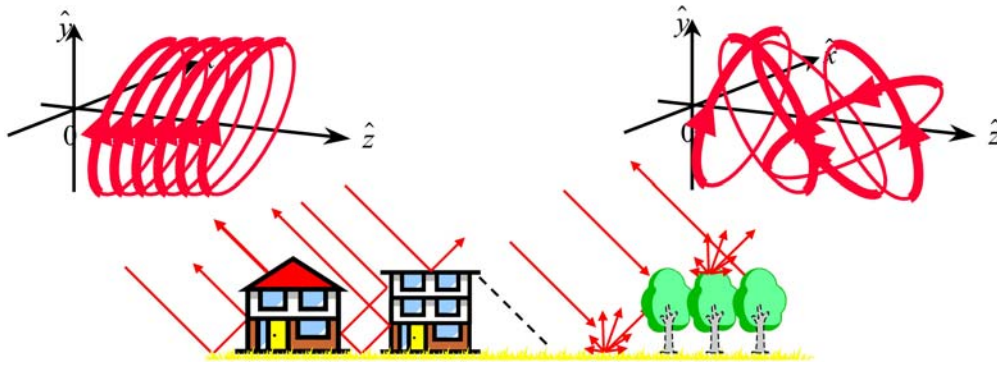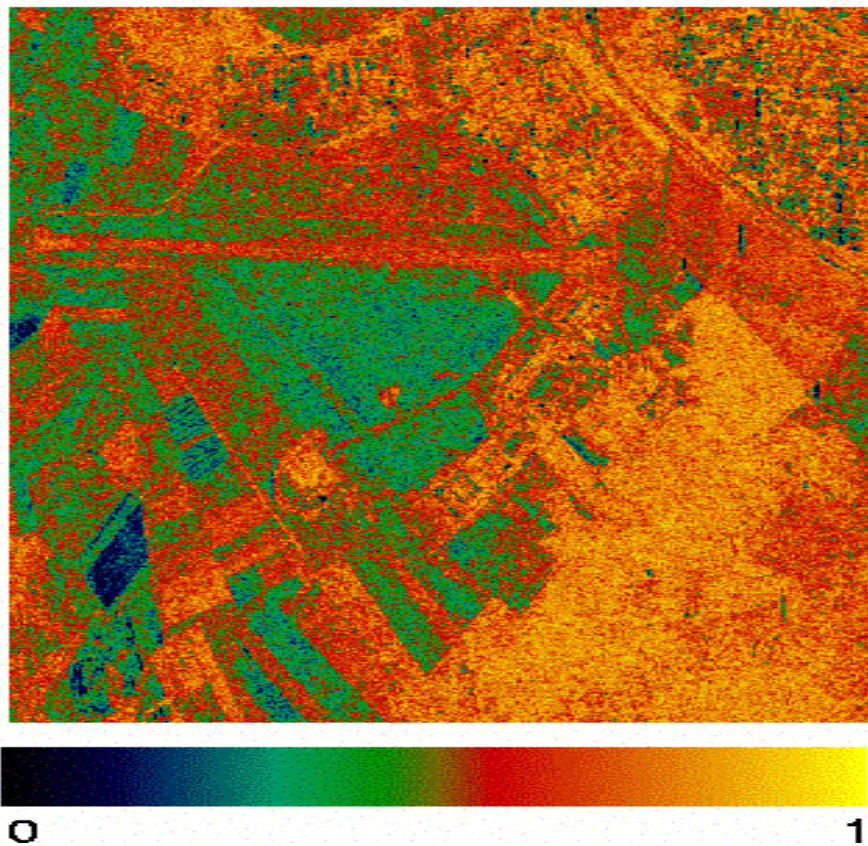
Figure 2a: Depolarisation and Entropy:

Figure 2b : Entropy image L-Band Oberpfaffenhofen, Germany DLR ESAR Data

5. Controlling Entropy: Volume Decorrelation in Radar Interferometry

Radar interferometry employs spatial separation by a baseline vector b of multiple sensors (for single-pass) or a single sensor at multiple times (for repeat-pass) [18]. It then uses phase difference as a proxy for elevation, enabling determination of scatterer height, hence leading to products such as high resolution digital elevation model (DEM) generation. Again however, the accuracy of this process is governed by phase stability or coherence. In this case we can define a coherency matrix as shown in equation 7

$$[J]_x = \begin{bmatrix} \langle p_x(\underline{r})p_x^*(\underline{r}) \rangle & \langle p_x(\underline{r})p_x^*(\underline{r}+\underline{b}) \rangle \\ \langle p_x(\underline{r})p_x^*(\underline{r}+\underline{b}) \rangle & \langle p_x(\underline{r}+\underline{b})p_x^*(\underline{r}+\underline{b}) \rangle \end{bmatrix}$$

(7)

where 'x' corresponds to a single selected polarisation channel. The presence of vegetation is now modelled as a finite bounded vertical random distribution of scatterers with a spatial weighting to account for the fact that scatterers deeper in the volume will have a smaller influence due to wave extinction. With this model, the coherence of vegetation can be expressed as shown in equation 8 [19,22]

$$\tilde{\gamma}_v e^{i\phi(z_o)} = \frac{\langle p_x(\underline{r})p_x^*(\underline{r}+\underline{b}) \rangle}{\sqrt{\langle p_x(\underline{r})p_x^*(\underline{r}) \rangle \langle p_x(\underline{r}+\underline{b})p_x^*(\underline{r}+\underline{b}) \rangle}} = e^{i\phi(z_o)} \frac{2\sigma_1 e^{i\phi(z_o)}}{\cos\theta_o(e^{2\sigma_1 h_v/\cos\theta_o}-1)} \int_0^h e^{ik_z z'} e^{\frac{2\sigma_1 z'}{\cos\theta_o}} dz'$$

$$= e^{i\phi(z_o)} \frac{p_1}{p_2} \frac{e^{p_2 h_v}-1}{e^{p_1 h_v}-1} \quad p_1 = \frac{2\sigma}{\cos\theta} \quad p_2 = p_1 + ik_z, \quad k_z = \frac{4\pi\Delta\theta}{\lambda\sin\theta} \approx \frac{4\pi B_n}{\lambda R\sin\theta}$$

(8)

where B_n is the normal component of the baseline to the line of sight. There are two key features of this model:

- Coherence (and therefore entropy) can now be controlled by selecting the baseline B_n.
- The interferometric coherence is independent of 'x' i.e. of polarisation

The first means that, unlike in polarimetry, we can now design the sensor to control the observed entropy of vegetation scattering (contrast equations 6 and 8). However, the second seems to indicate that we do not need polarisation diversity, as equation 8 does not change with 'x'. Why then do we need to consider POLInSAR? The answer to this apparent contradiction is hidden in equation 8 itself. We see that the coherence is a function of several parameters, the unknown height of the vegetation , the unknown wave extinction and the unknown ground topographic phase. It follows that one channel of interferometry by itself cannot be used for unambiguous parameter retrieval. The situation is further complicated by the fact that for microwaves the extinction can be relatively small and hence there can be penetration of vegetation right down to the underlying surface. This requires us to consider combined surface and volume scattering, so forcing us to modify equation 8 to at least a two-layer model as shown in equation 9 [19,20,21,22].

$$\tilde{\gamma}_x = e^{i\phi(z_o)} \frac{\tilde{\gamma}_v + \mu_x}{1 + \mu_x}$$

(9)

where μ_x is the ratio of surface-to-volume scattering, which changes with frequency, vegetation density and surface conditions. However, it is now that polarisation diversity helps, as from figure 2b we see that surface scattering has low entropy and hence we can control its influence in 9 by changing 'x' at the same time as leaving the volume coherence unchanged. Consequently by using POLInSAR we can increase the number of observations faster than the number of unknowns and hence achieve parameter estimation with a coherence or entropy under our control. This is one reason why there is such an interest in developing POLInSAR sensors for vegetation mapping [22,23,24]. Several further examples can be found as part of the proceedings of a recent ESA funded workshop focussing on this topic (http://earth.esa.int/polinsar/).

Figure 3 shows an example POLInSAR product, obtained using the L-band airborne E-SAR sensor operated by DLR in Germany. Here we show a radar-derived quantitative tree height estimation overlaid on a radar-derived DEM. It uses the model of equation 9 with polarisation diversity over 'x' to isolate the height h_v and $\phi(z_0)$ dependence and provide a map of tree height over the mountainous

terrain. Quantitative comparisons with in-situ measurements indicate an accuracy of height estimation around 10%. [21,22,24]. While tree height is itself a useful product, it can also provide the basis for various important secondary products. For example, in Figure 4 we show a forest biomass map derived using the height data in Figure 3 coupled to allometric equations derived from forestry tables for this region [24]. In the upper Figure we also show a conventional SAR image of the scene, which displays
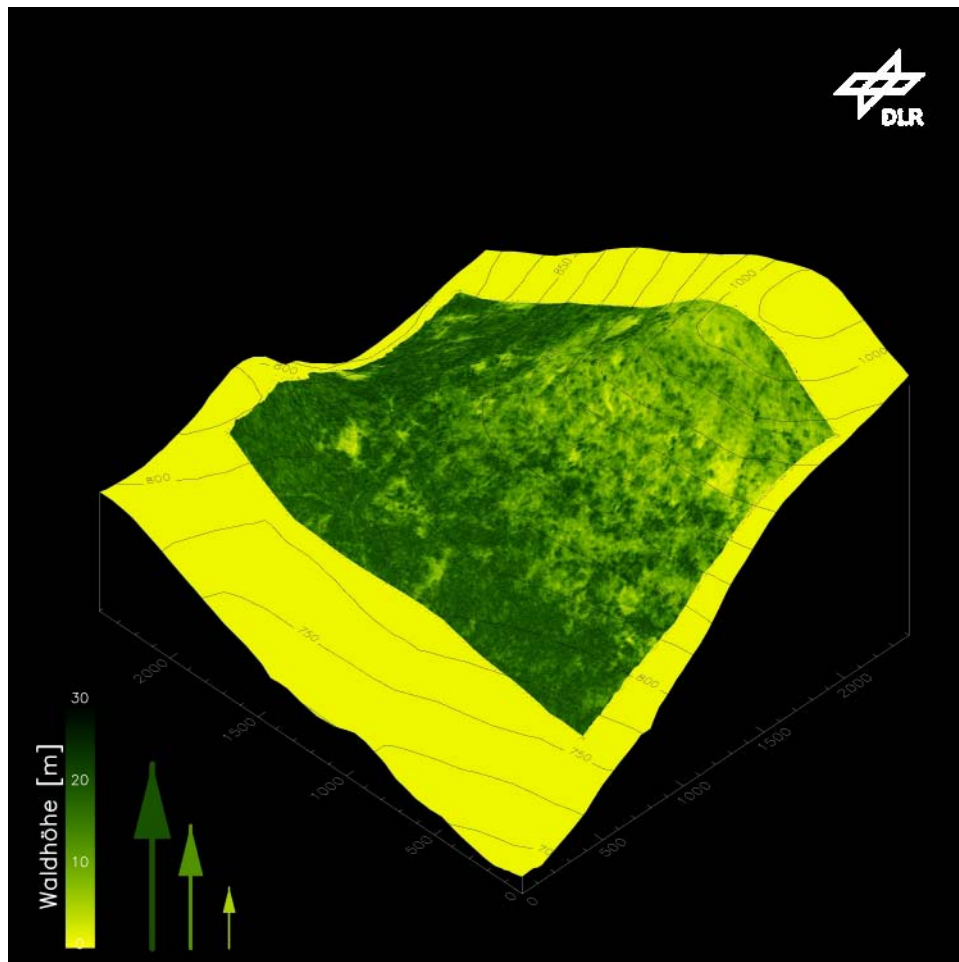

Figure 3: Tree Height and Topography Estimated using L-Band
DLR E-SAR Polarimetric Interferometric Data

none of the important forest structural information seen in the height/biomass products. This nicely illustrates the potential 'information gain' obtained by using POLInSAR sensors for vegetation applications.
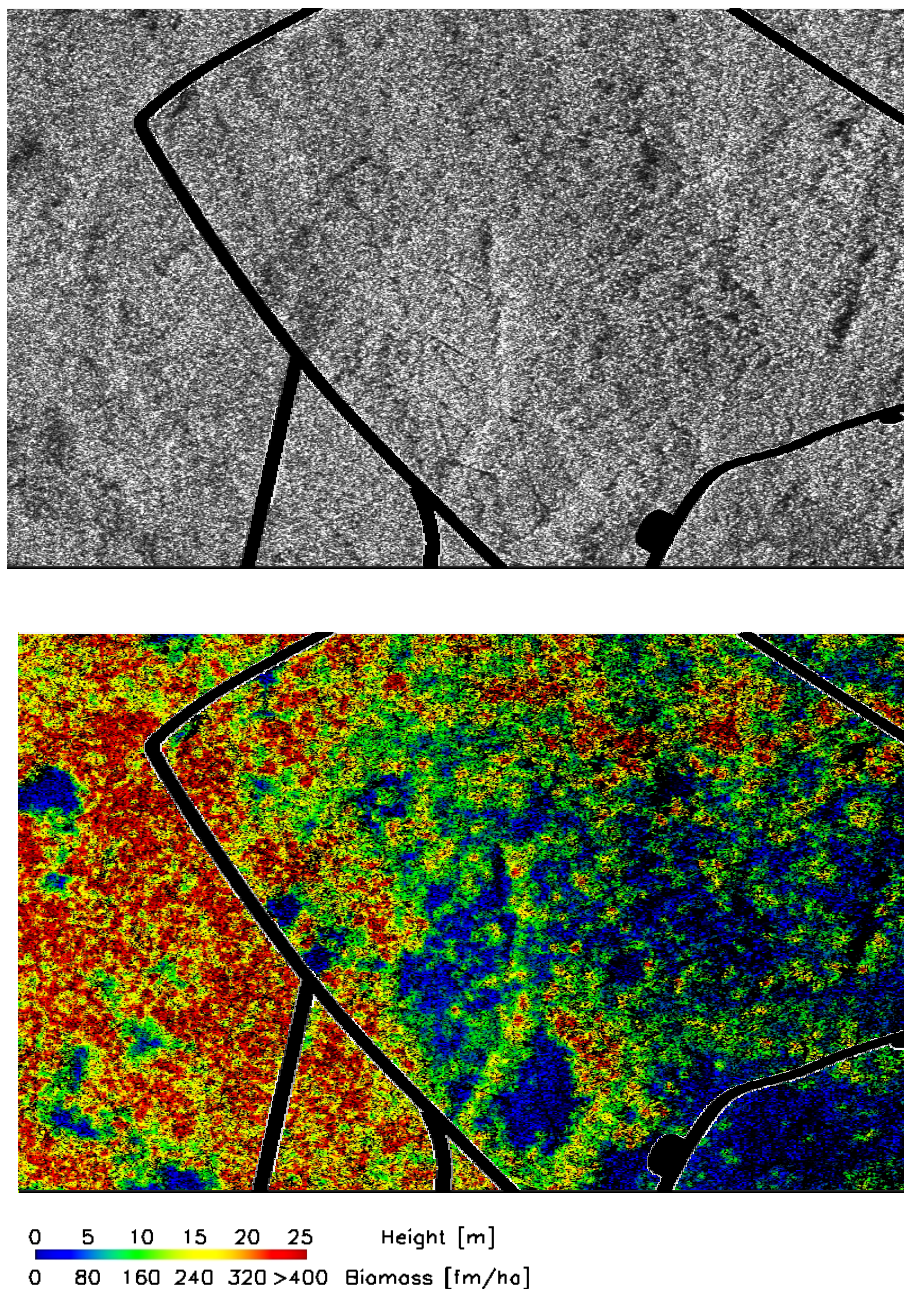
Figure 4 : HH RCS image (upper) and radar derived tree height/biomass map
for the same scene (lower) (see reference [24])

6. Conclusions and Future Developments

In this treatment we have developed as a theme the importance of multi-channel phase in radar remote sensing and used it to support the idea of combining polarisation diversity with interferometry in future radar sensors. Key to success is the generalised coherence or entropy and key to robustness the development of physical models for the interaction of polarised waves with natural surfaces. We have concentrated on one important example, namely tree height and biomass estimation, but there are many other application areas where this technology is being considered. Table I provides a selective survey of different geo-physical parameters and examples of the types of algorithms currently being developed. We can see that polarimetric and/or interferometric phase appears in every area. This table provides a 'snapshot' in time, each area is ongoing in research and development and exciting future

technology innovations such as bistatic radar and satellite radar constellations will require parallel improvements in our understanding of the interaction of polarised waves with natural media in order to fully exploit the scientific and commercial potential of radar in remote sensing.

By using more than 2 polarimetric data sets polarimetric interferomerty can be extend to more complex approaches. One of possible approache is differential polarimetric interferometry. By using 3 or more temporal separated data sets it could be possible to enhance the potential of conventional differential interferometry by using the polarimetric information in order to analyse the changes in scattering processes over time. POL-IN-SAR imaging, when applied to 'Repeat-Pass Image Overlay Interferometry', provides differential background validation and measurement, stress assessment, and environmental stress-change monitoring capabilities.

Another approach currently under investigation is polarimetric SAR tomography, which is the extension of conventional two-dimensional SAR imaging principle to three dimensions. A real three-dimensional imaging of a scene is achieved by the formation of an additional synthetic aperture in elevation by a coherent cobination of images acquired from several parallel flight tracks. It can be seen as a direct approach to resolve the SAR scattering ambiguity problems. The introduction of tomographic SAR offers the possibility of a direct localisation and identification of all scattering contributions in a volume. This greatly extends the potential of SAR, particularly for the analysis of volume structures like for example forests as shown in Figure 5.
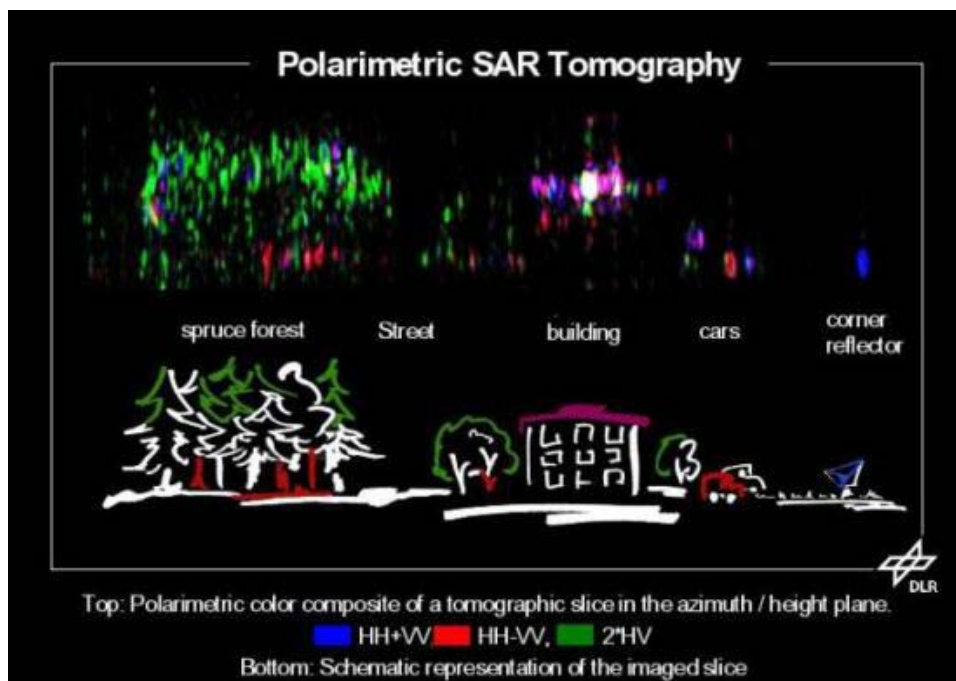

Figure 5 Tomographic slice generated from 13 parallel flight tracks with a mutual distance of 20m. Sensor: DLR ESAR in L-band. Scene: Onberpfaffenhofen, Germany. (Reigber[25])

7. Acknowledgements

Product	Radar Parameter	Polarimetric and Interferometric Measurement Parameters	Source Ref.
Bare Surface Roughness	$0 \le R(ks) \le 1$ s=rms roughness k=wavenumber=$2\pi/\lambda$	$R = \dfrac{\left\langle \left\|S_{HH}-S_{VV}\right\|^2\right\rangle - 4\left\langle\left\|S_{HV}\right\|^2\right\rangle}{\left\langle \left\|S_{HH}-S_{VV}\right\|^2\right\rangle + 4\left\langle\left\|S_{HV}\right\|^2\right\rangle}$	10,11,15
Bare Surface Moisture	$0 \le M(\theta,\varepsilon_r) \le 1$ θ = angle of incidence ε_r – dielectric constant	$M = \dfrac{\left\langle \left\|S_{HH}-S_{VV}\right\|^2\right\rangle + 4\left\langle\left\|S_{HV}\right\|^2\right\rangle}{\left\langle \left\|S_{HH}+S_{VV}\right\|^2\right\rangle}$	10,11,15
Surface Slope	$\tan\beta = \dfrac{\tan\omega}{\sin\bar\phi - \cos\bar\phi\,\tan\gamma}$ $\tan\gamma$ = range slope $\tan\omega$ = azimuth slope $\bar\phi$ = radar look angle	$\phi = \tan^{-1}\left(\dfrac{2\,\text{Re}\left\langle (S_{HH}-S_{VV}).S_{HV}^*\right\rangle}{4\left\langle\left\|S_{HV}\right\|^2\right\rangle - \left\langle\left\|S_{HH}+S_{VV}\right\|^2\right\rangle}\right)$ $-\dfrac{\pi}{4} \le \beta = \begin{cases} \dfrac{\phi+\pi}{4} & \text{if } \phi \le \dfrac{\pi}{4} \\ \dfrac{\phi+\pi}{4}-\dfrac{\pi}{2} & \text{if } \phi > \dfrac{\pi}{4} \end{cases} \le \dfrac{\pi}{4}$	12,14
True Ground Topography	$z_o = z_{ref} + \dfrac{\hat\phi}{k_z}$ $k_z = \dfrac{4\pi\Delta\theta}{\lambda\sin\theta} \approx \dfrac{4\pi B_n}{\lambda R\sin\theta}$	$\hat\phi = \arg(\tilde\gamma_{HH-VV} - \tilde\gamma_{HV}(1-L))$ $A = \left\|\tilde\gamma_{HV}\right\|^2 - 1,$ $B = 2\,\text{Re}((\tilde\gamma_{HH-VV} - \tilde\gamma_{HV}).\tilde\gamma_{HV}^*),$ $C = \left\|\tilde\gamma_{HH-VV} - \tilde\gamma_{HV}\right\|^2$ $AL^2 + BL + C = 0 \Rightarrow \hat L$	21,22,23
Vegetation Component Structure	$m = \begin{cases} >1 & \text{prolate particles} \\ 1 & \text{spherical particles} \\ <1 & \text{oblate particles} \end{cases}$ $P = \dfrac{m\varepsilon_r + 2}{m + \varepsilon_r + 1}$	$V = \dfrac{4\left\langle\left\|S_{HV}\right\|^2\right\rangle}{\left\langle\left\|S_{HH}+S_{VV}\right\|^2\right\rangle}$ $\Rightarrow a = (1-2V), b = -2(1+3V), c = (1-7V)$ $\Rightarrow aP^2 + bP + c = 0 \Rightarrow \hat P$	4,16,17
Vegetation Height and Extinction	h_v = top height in m σ = mean extinction (m^{-1}) θ = angle of incidence $\hat\phi$ = ground topographic phase (see above)	$\min_{h_v,\sigma} L_1 = \left\| \tilde\gamma_{HV} - e^{i\hat\phi}\dfrac{p}{p_1}\dfrac{e^{p_1 h_v}-1}{e^{ph_v}-1} \right\|$ where $\begin{cases} p = \dfrac{2\sigma}{\cos\theta} \\ p_1 = p + ik_z \end{cases}$	20,21,22

Table I : Examples of Geophysical Parameter Estimation using Radar Polarimetry and Interferometry

8. References

[1] Boerner W M et al "Polarimetry in Remote Sensing: Basic and Applied Concepts", Chapter 5 in Manual of Remote Sensing, Vol. 8, 3rd edition, F M Henderson, A J Lewis eds. New York, Wiley, 1998

[2] Cloude S R, E. Pottier, "A Review of Target Decomposition Theorems in Radar Polarimetry", IEEE Transactions on Geoscience and Remote Sensing, Vol. 34 No. 2, pp 498-518, March 1996

[3] Freeman A, S.L. Durden, "A Three Component Model for Polarimetric SAR Data", IEEE Transactions on Geoscience and Remote Sensing, Vol. GE-36, pp. 963-973, 1998

[4] Cloude S R, E. Pottier, "An Entropy Based Classification Scheme for Land Applications of Polarimetric SAR", IEEE Transactions on Geoscience and Remote Sensing, Vol. 35, No. 1, pp 68-78 , January 1997

[5] van Zyl J J "Unsupervised Classification of Scattering Behaviour Using Radar Polarimetry Data", IEEE Transactions on Geoscience and Remote Sensing, Vol. GE-27(1), 1990, pp 36-45

[6] Born M, E Wolf "Principles of Optics", Chapters 1, 10, Pergamon Press, 6th Edition, 1989, ISBN 0-08-026428-4

[7] Touzi R, A Lopes, J Bruniquel, P W Vachon,"Coherence Estimation for SAR Imagery", IEEE Transactions Geoscience and Remote Sensing, Vol. 37/1, pp 135-149, January 1999

[8] Freeman A., S Saatchi, "Effects of Faraday Rotation on Backscatter Signatures in SAR Image data", Proc. SPIE, vol 3120, pp 37-44, 1997

[9] Quegan S "A Unified Algorithm for Phase and Cross-talk calibration of Polarimetric Data-theory and Observations", IEEE Trans GRS-32, Jan 1994, pp 89-99

[10] Hajnsek I., E. Pottier, S.R. Cloude", Inversion of Surface Parameters from Polarimetric SAR", IEEE Transactions on Geoscience and Remote Sensing, Vol 41/4, April 2003, pp 727-744

[11] Hajnsek I., Papathanassiou, K. P. & Cloude, S. R., 'Surface Parameter Estimation Using fully polarimetric L- and P-band Radar data', Proc. 3rd International Symposium, 'Retrieval of Bio-Geophysical Parameters from SAR Data for Land Applications', 11-14 Sept. 2001, Sheffield, UK, ESA SP-475, January 2002, pp. 159-164

[12] Lee J.S., D L Schuler, T L Ainsworth, "Polarimetric SAR Data Compensation for Terrain Azimuth Slope Variation", IEEE Trans. Geoscience and Remote Sensing, Vol 38/5, pp 2153-2163, September 2000

[13] Lee J.S., M.R. Grunes, T.L .Ainsworth, L. J. Du, D. L. Schuler, S.R Cloude, "Unsupervised Classification using Polarimetric Decomposition and the Complex Wishart Distribution", IEEE Transactions Geoscience and Remote Sensing, Vol 37/1, No. 5, p 2249-2259, September 1999

[14] Schuler D, T. Ainsworth, J.S. Lee, G. De Grandi, "Topographic Mapping using Polarimetric SAR data", International Journal of Remote Sensing, Vol. 34, no. 5, pp 1266-1277, 1998

[15] Cloude S.R., D G Corr, "A New Parameter for Soil Moisture Estimation", Proceedings of IEEE International Geoscience and Remote Sensing Symposium (IGARSS 2002), Toronto, Canada, Vol. 1, pp 641-643, July 2002

[16] Cloude S.R., J. Fortuny, J.M. Lopez, A. J. Sieber, "Wide Band Polarimetric Radar Inversion Studies for Vegetation Layers", IEEE Transactions on Geoscience and Remote Sensing, Vol 37/2 No 5, pp 2430-2442, September 1999

[17] Cloude S R, "Helicity in Radar Remote Sensing", Proceedings of IEEE International Geoscience and Remote Sensing Symposium (IGARSS 2002), Toronto, Canada, Vol.1, pp 411-413, July 2002

[18] Bamler R, P. Hartl, "Synthetic Aperture Radar Interferometry", Inverse Problems, 14, R1-R54, 1998

[19] Treuhaft R N, P. Siqueria, "Vertical Structure of Vegetated Land Surfaces from Interferometric and Polarimetric Radar", Radio Science, Vol. 35(1), pp 141-177, January 2000

[20] Cloude S R, K P Papathanassiou, "Polarimetric SAR Interferometry", IEEE Transactions on Geoscience and Remote Sensing, Vol 36. No. 5, pp 1551-1565, September 1998

[21] Papathanassiou K.P., S.R. Cloude, "Single Baseline Polarimetric SAR Interferometry", IEEE Transactions Geoscience and Remote Sensing, Vol 39/11, pp 2352-2363, November 2001

[22] Cloude S.R. , K.P. Papathanassiou, " A 3-Stage Inversion Process for Polarimetric SAR Interferometry", IEE Proceedings, Radar, Sonar and Navigation, Volume 150, Issue 03, June 2003, pp 125-134

[23] Yamada H, Y Yamaguchi, E Rodriguez, Y Kim, W M Boerner, "Polarimetric SAR Interferometry for Forest Canopy Analysis by Using the Super-resolution Method", IEICE Transactions on Electronics, VOL.E84-C, No.12, 2001, pp1917-1924, December 2001

[24] Mette T., I. Hajnsek, K. P. Papathanassiou, R Zimmerman, " Above Ground Forest Biomass Estimation using Fully Polarimetric/Interferometric Radar Data", Proceedings of ESA Workshop, POLInSAR –Applications of SAR Polarimetry and Polarimetric Interferometry, Frascati, Italy, January 2003, SP-529, http://www.earth.esa.int/polinsar

[25] Reigber A.,"Airborne Polarimetric SAR Tomography", DLR Report No. 2002-2, PhD thesis University of Stuttgart, Germany 2001

Appendix A:
POLInSAR Applications In Remote Sensing

This appendix is part of a REVIEW presented at the Tutorial on Radar Interferometry and Polarimetry performed at 23.05.2004 in connection with 5. European Conference on Synthetic Aperture Radar (EUSAR), 24.05.2004 - 27.05.2004, Ulm, Germany, by Shane R. Cloude (School of Electrical and Electronic Engineering University of Adelaide, South Australia, 5005, Australiae-mail : scloude@eleceng.adelaide.edu.au); Compare:VDE.com/ITG

A.1. INTRODUCTION

Polarimetric SAR Interferometry (POLInSAR) was first developed for applications in remote sensing in 1997 using SIRC L-Band data [1,2]. In its original form it involved generating phase differences between interferograms formed using different polarization combinations. These phase differences were later observed to be correlated with vegetation height [2]. However, it was quickly realized that more accurate estimates of height could be obtained by correcting the phase differences using coherent wave scattering models [3,4,6]. Since then there have been several groups working on the development and inversion of suitable models for the interpretation of POLInSAR data. A particularly useful model, which presents a good compromise between physical structure and model complexity is a variant of that first developed by Treuhaft et al [3,4]. This 2-layer model is widely used in interferometric SAR (InSAR) applications. Here we review its main structure and importance in POLInSAR.

The basic radar observable in POLInSAR is the 6x6 coherency matrix of a pixel, defined as shown in equation 1

$$\left\langle \underline{k}\,\underline{k}^{*T} \right\rangle = \begin{vmatrix} T_{11} & \Omega_{12} \\ \Omega_{12}^{*T} & T_{22} \end{vmatrix} \qquad \underline{k} = \frac{1}{\sqrt{2}} \left[S_{hh}^1 + S_{vv}^1 \quad S_{hh}^1 - S_{vv}^1 \quad 2S_{hv}^1 \quad S_{hh}^2 + S_{vv}^2 \quad S_{hh}^2 - S_{vv}^2 \quad 2S_{hv}^2 \right]^T \qquad -1)$$

where superscripts 1 and 2 denote measurements at the two ends of the baseline. We have further partitioned the matrix into 3 x 3 polarimetric coherency matrices T_{ii} and polarimetric inteferometry $\Omega_{\iota\varphi}$. Generally this matrix must be estimated by multi-look processing of the data using a local window centred on the pixel of interest. Consequently, full matrix estimation follows a complex Wishart distribution and this enables characterisation of the fluctuation statistics in POLInSAR data [5]. According to the 2-layer vegetation model, first derived in [4] and extended for fully polarimetric interpretation in [6], the complex interferometric coherence for a random volume over a ground can be derived as shown in equation 2 and shown schematically in figure 1 where $\underline{w}$ is a 3 component unitary complex vector defining the choice of polarization [2], σ the mean wave extinction in the medium, k_z the vertical wavenumber of the interferometer (following spectral range filtering) and θ the mean angle of incidence. The angles ϕ_1 and ϕ_2 are the phase centres of the bottom of layers 1 and 2 respectively.
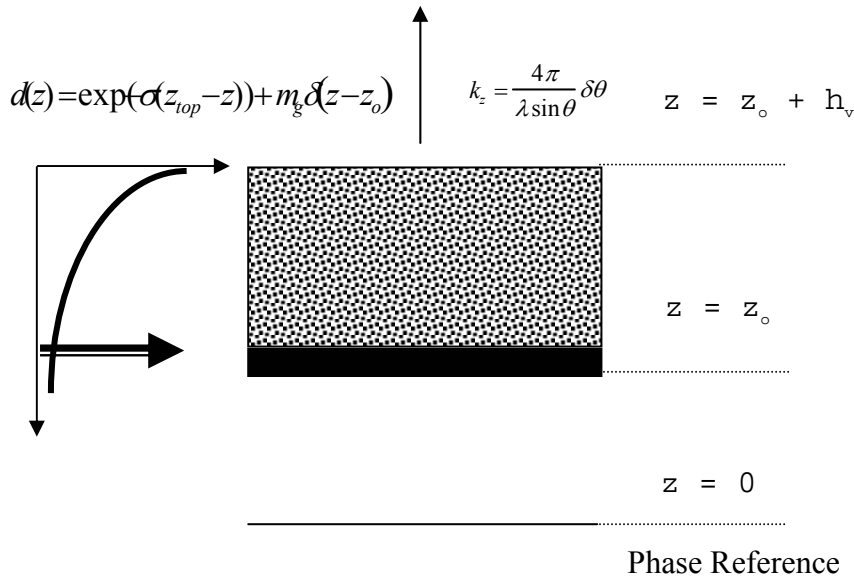

Figure 1: Schematic representation of the 2-Layer coherence model for vegetated land surfaces

$$\tilde{\gamma} = \frac{\underline{w}^{*T} \Omega_{12} \underline{w}}{\underline{w}^{*T} T_{11} \underline{w}} \qquad - 2)$$

$$T_{11} = I_1^V + e^{-\frac{2\sigma h_v}{\cos\theta_o}} I_1^G \qquad \Omega_{12} = e^{i\phi_2} I_2^V + e^{i\phi_1} e^{-\frac{2\sigma h_v}{\cos\theta_o}} I_2^G$$

$$I_1^V = e^{-\frac{2\sigma h_v}{\cos\theta}} \int_0^h e^{\frac{2\sigma z'}{\cos\theta_o}} T_V dz' \qquad I_1^G = \int_0^h \delta(z') e^{\frac{2\sigma z'}{\cos\theta_o}} T_g dz' = T_g$$

$$I_2^V = e^{-\frac{2\sigma h_v}{\cos\theta}} \int_0^h e^{\frac{2\sigma z'}{\cos\theta_o}} e^{ik_z z'} T_V dz' \qquad I_2^G = T_g$$

Within figure:
$$d(z) = \exp(-\sigma(z_{top} - z)) + m_g \delta(z - z_o) \qquad k_z = \frac{4\pi}{\lambda \sin\theta} \delta\theta \qquad z = z_o + h_v$$

$$z = z_o$$

$$z = 0$$

Phase Reference

T_v is the 3 x 3 diagonal coherency matrix for the volume scattering and T_g the reflection symmetric ground scattering coherency matrix, defined as shown in equation 3 [6]

$$T_V = m_v \begin{vmatrix} 1 & 0 & 0 \\ 0 & \mu & 0 \\ 0 & 0 & \mu \end{vmatrix} \quad 0 \le \mu \le 0.5 \quad T_g = m_g \begin{vmatrix} 1 & t_{12} & 0 \\ t_{12}^* & t_{22} & 0 \\ 0 & 0 & t_{33} \end{vmatrix} \qquad - 3)$$

This two-layer model is supported by radar tomographic experiments at L-band [7,8]. For example, figure 2 shows vertical profiles for 20m high spruce stands in the three polarization channels [8]. Note the similarity to figure 1 and the distinct ground signal, with a minimum in the HV channel. Each profile was obtained as a lateral average at each vertical position. Closer examination of the relative profiles shows that $<|2*HV|>^2 = <|HH-VV|>^2$ as expected for the random volume assumption in figure 1 and T_v in equation 3. This supports the use of a random rather than an oriented volume for L-band forest remote sensing.
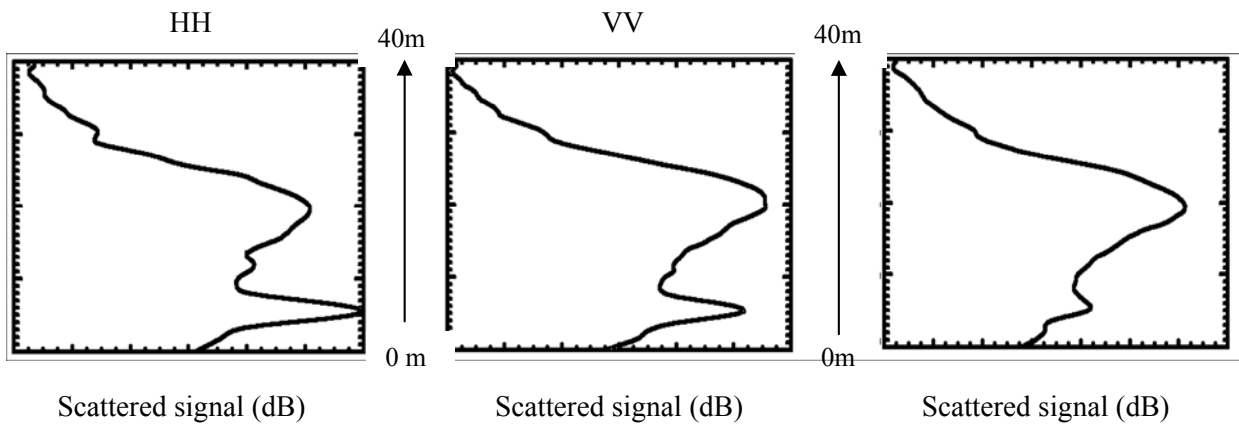

Figure 2: Vertical profiles of L-band Spruce forest scattering from polarimetric radar tomography [8]

Further, by assuming that the canopy extends from crown to ground then we can simplify equation 2 by setting $\phi_1 = \phi_2$. Later we shall examine the consequences of this assumption, but for the moment we assume the bottom of the canopy corresponds to the ground surface.

By combining equations 2 and 3 we obtain the following explicit equation for the complex coherence

$$\tilde{\gamma} = \frac{\underline{w}^{*T}(e^{i\phi_1}I_2^V + e^{-\frac{2\sigma h_v}{\cos\theta_o}}T_g e^{i\phi_1})\underline{w}}{\underline{w}^{*T}(I_1^V + e^{-\frac{2\sigma h_v}{\cos\theta_o}}T_g)\underline{w}} = \frac{\underline{w}^{*T}(e^{i\phi_1}v^{-1}I_2^V + e^{i\phi_1}v^{-1}T_g)\underline{w}}{1 + \underline{w}^{*T}v^{-1}T_g \underline{w}} \qquad v^{-1} = \frac{1}{\underline{w}^{*T}I_1^V \underline{w}} \qquad - 4)$$

which can be rewritten as the equation of a straight line in the complex plane as

$$\hat{\gamma}(\underline{w}) = e^{i\phi_1}\frac{\hat{\gamma}_v + \mu(\underline{w})}{1 + \mu(\underline{w})} = e^{i\phi_1}\left(\hat{\gamma}_v + \frac{\mu(\underline{w})}{1 + \mu(\underline{w})}(1 - \hat{\gamma}_v)\right)$$

$$= e^{i\phi_1}(\hat{\gamma}_v + L(\underline{w})(1 - \hat{\gamma}_v)) \qquad 0 \le L(\underline{w}) \le 1 \qquad - 5)$$

where the ground-to-volume scattering ratio μ includes the effects of wave extinction in the medium and is defined as

$$\mu(\underline{w}) = \frac{2\sigma}{\cos\theta_o (e^{\frac{2\sigma h_v}{\cos\theta_0}} - 1)} \frac{\underline{w}^{*T} T_g \underline{w}}{\underline{w}^{*T} T_V \underline{w}} \geq 0 \qquad - 6)$$

Note that μ is positive semi-definite and that the max/min values of this function versus polarization are given by the eigenvalues of a contrast optimization problem since

$$\max_{\underline{w}} \frac{\underline{w}^{*T} T_B \underline{w}}{\underline{w}^{*T} T_A \underline{w}} \quad \Rightarrow \quad T_A^{-1} T_B \underline{w}_{opt} = \mu \underline{w}_{opt} \qquad - 7)$$

The eigenvalues μ_i are non-degenerate, due to the strong polarization dependence of ground scattering, and this lends support to the variation of coherence with polarization in equation 4. We note that the three eigenvectors of this problem are not mutually orthogonal. This is in contrast to the situation when differential propagation effects are important, when the optimum $\underline{w}$ vectors are related to the propagation eigenpolarisations, which for a single vegetation layer are mutually orthogonal [10,11]. Note also that for a reflection symmetric ground with azimuthally symmetric vegetation cover (as implied by equation 3), the minimum eigenvalue will be obtained for the HV channel. In the more general case, the coherence optimizer [1,2] can be used to find the max and min ground components in equation 6.

Consequently, in equation 5 only μ is a function of polarisation. This arises since γ_v is a polarization independent volume integral as shown in equation 8.

$$\hat{\gamma}_v = \frac{\underline{w}^{*T} \int_0^{h_v} e^{\frac{2\sigma z'}{\cos\theta_o}} e^{ik_z z'} T_V dz' \underline{w}}{\underline{w}^{*T} \int_0^{h_v} e^{\frac{2\sigma z'}{\cos\theta_o}} T_V dz' \underline{w}} = \frac{m_v \int_0^{h_v} e^{\frac{2\sigma z'}{\cos\theta_o}} e^{ik_z z'} dz'}{m_v \int_0^{h_v} e^{\frac{2\sigma z}{\cos\theta_o}} dz'} = \frac{2\sigma}{\cos\theta_o (e^{2\sigma h_v/\cos\theta_o} - 1)} \int_0^{h_v} e^{ik_z z'} e^{\frac{2\sigma z'}{\cos\theta_o}} dz' \qquad - 8)$$
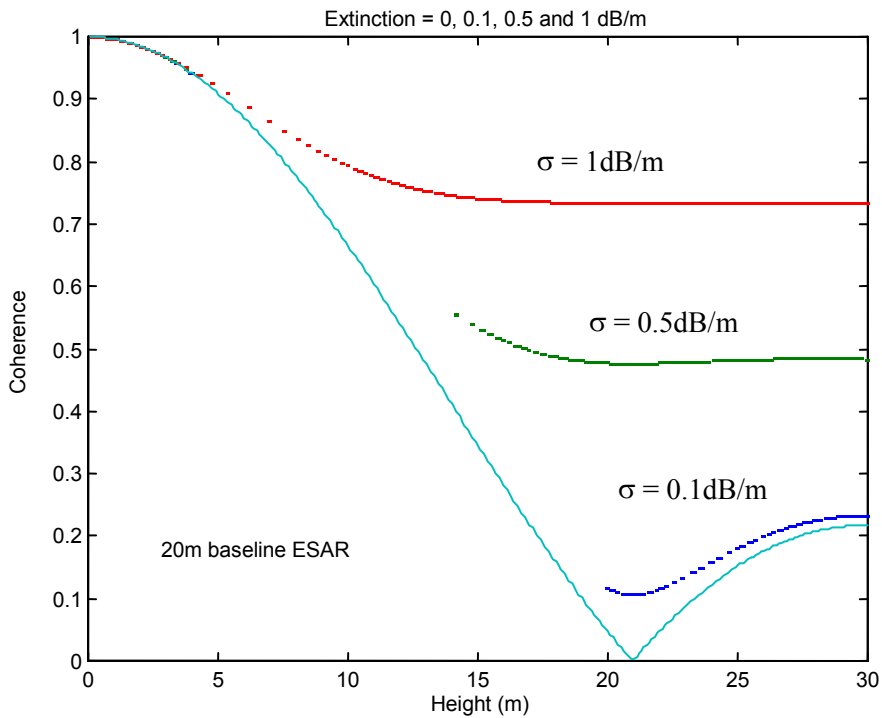

Figure 3 : Coherence variation versus tree height and mean extinction

In the limit that the wave extinction is zero this reduces to an elementary sinc function. Figure 3 shows how the volume coherence varies as a function of vegetation height and extinction for a vertical wavenumber kz = 0.2 (corresponding to a 20m baseline at L band for the DLR E-SAR airborne system. Note that the coherence falls with increasing vegetation height as a consequence of volume decorrelation. However, the effect of unknown extinction makes the relationship between coherence and height ambiguous.

As well as the coherence amplitude, consideration must also be given to variation of the phase of the observed interferogram. According to equation 8, the presence of vegetation causes an offset in the estimation of the interferometric phase of the ground topography given by half the vegetation height (or more as the extinction increases). This offset decreases with increasing ground component but is always present, biasing the estimation of ground topography. Note that the above vegetation-plus-ground scattering model makes no restrictions about the observed phase difference between the elements of a single scattering matrix. These relative polarimetric phase differences are caused by a polarisation dependent scattering phase term introduced by the scatterer and cancel each other when an interferogram is formed by using the same polarisation at both ends of the baseline. This is not the case when the interferogram is formed by using different polarisations at either end of the baseline. In this case topographic and scattering related coherence and phase information is mixed. Hence care is required to distinguish the polarimetric interferometric and polarimetric phase angles. This distinction was overlooked in [9], where the authors proposed a relationship between these two phase angles which has only limited validity.

Inversion of equation 5 is greatly facilitated by employing a geometrical interpretation inside the unit circle of the complex coherence plane. Figure 4 shows how the model maps coherence points from equation 5 onto a line in the complex plane. This line has three important features:
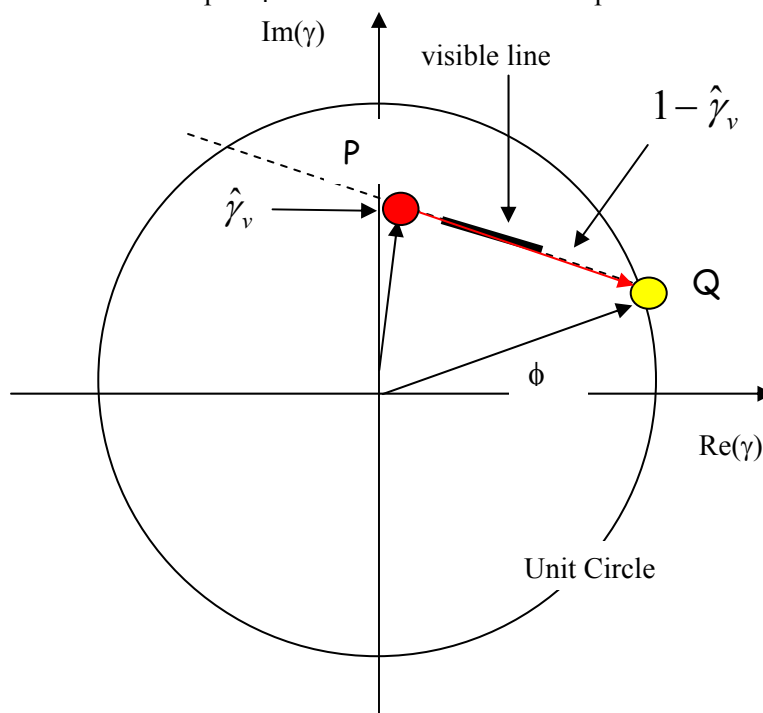

Figure 4: The line model for polarimetric variation of interferometric coherence

1) The line intersects the circle at 2 points. One of these is the underlying topography related phase (shown as the point Q in figure 4). The other is a false solution and must be rejected by the inversion process.

2) The volume coherence γ_ϖ lies at one end of the line ($\mu = 0$). It is shown as the point P in figure 3. This point is central to the estimation of height and extinction and needs to be estimated from the data

3) The visible length of the line in the data may only be a fraction of PQ and neither P nor Q may be directly observed. The visible length depends on baseline, operating frequency and vegetation density [6]. However the line can be extrapolated to enable parameter estimation as we now show.

A.2. POLINSAR Model Inversion

Inversion of equation 5 involves taking observations of the complex coherence at a number of different polarizations and then minimizing the difference between the model predictions and observations in a least squares sense. In most previous studies [6] this has been implemented as a six-dimensional optimisation problem using standard iterative procedures. Due to the non-linear nature of the optimisation problem, the obtained solution depends strongly on the choice of the starting values. Poor starting values may lead to ambiguous and/or unstable parameter estimates [15,17,18,19]. However, we can clarify the requirements of the inversion by breaking the process down into three separate stages as follows:

Stage 1 : Least Squares Line Fit

The first stage is to find the best-fit straight line inside the unit circle of interferometric coherence. To do this we vary two phase variable ψ_1 and ψ_2 as shown in figure 5.
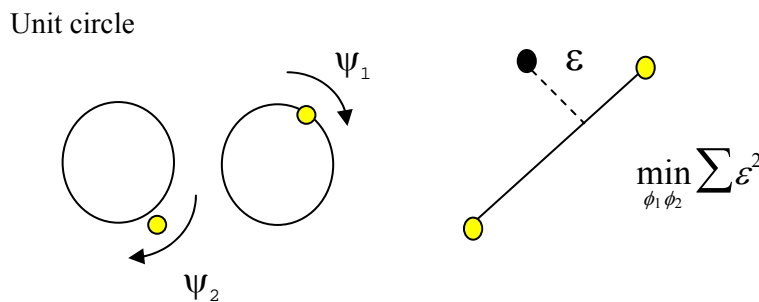

Figure 5: Phase-based least square line fit

Each pair defines a line and we choose the pair that minimises the MSE between the line and set of coherence points as shown. One way to do this is to use a total least squares line fit to the real and imaginary components of the data and then use the line parameter estimates to secure the intersection points. Alternatively a faster least squares line fit in the real and/or imaginary parts can secure an estimate of the minimum error solution [14]. An alternative method based on a maximum likelihood approach using the complex Wishart distribution has recently been outlined in [21]. Phase centre estimation based on the ESPRIT processing technique has also been employed for this purpose [22].

2) Coherence bias for low coherence values. Standard boxcar methods overestimate low coherence values and hence distort the line parameters [13]. Either unbiased estimators should be used or the interferometer design should avoid low values of coherence through judicious choice of the baseline. The bias reduces with increasing coherence and with increasing N.

3) SNR variations can cause loss of coherence, again distorting the line. This is a potentially serious issue as SNR is generally a function of polarisation. Fortunately, such variations are seen mainly in surface scattering and light vegetation cover and not in forestry applications.

4) Temporal decorrelation. In repeat-pass systems, coherence can fall due to changes in the scene between passes. To avoid this, single pass polarimetric interferometry is preferred. We note from

equation 1 that volume temporal decorrelation effects will not necessarily destroy the line structure, only lower the coherence so causing additional problems through 1) and 2) above. For example, in the presence of wind driven vegetation decorrelation, only the coherent volume integral factor I_2^V in equation 2 is modified. The effect is to reduce the coherence magnitude without changing the phase of the integral. This can be modelled as a multiplicative scalar factor γ_t, the temporal decorrelation and equation 5 must then be modified as shown in equation 10.

This remains the equation of a straight line and both ϕ and μ are invariant to such transformations. However the height/extinction estimation becomes ambiguous. Regularisation of the solution can be

$$\tilde{\gamma} = e^{i\phi}\left(\gamma_t \tilde{\gamma}_v - \frac{\mu}{1+\mu}\left(1 - \gamma_t \tilde{\gamma}_v \right) \right) \qquad\qquad - \ 10)$$

achieved by assuming a fixed value for the mean extinction, as we show later. A second problem is that the coherence values decrease and this increases the variance of the phase/coherence estimates according to equation 9.

5) Even if all other factors 1-4 are minimised, the line model assumption may not be correct. This can arise for several reasons, such as when the vegetation becomes oriented and we have differential extinction and propagation phase. In this case the volume coherence itself becomes a function of polarisation. A suitable statistical confidence test for the line can be applied as shown in [14]. Oriented volume effects can also be identified through the presence of orthogonal eigenvectors and the rank order of the coherence values. [10,11]. Recently a technique for determining the coherence region shape has been developed [20] although in its current form it takes no account of the intrinsic statistical fluctuations in interferometric coherence and phase data. The output from stage 1 is then a set of ψ_1,ψ_2 paired values for each pixel. The next stage involves deciding which of these is the true ground phase through the process of vegetation bias removal.

Stage 2 : Vegetation Bias Removal

In the second stage we must choose one of the pair ψ_1,ψ_2 as the underlying ground topographic phase for each pixel. To do this we extract the line from figure 4 and mark the polarization states in rank order as shown schematically in figure 6. It follows from equation 4 that the ground-to-volume ratio μ is given by the distance along the line as shown in figure 6. We see that the nearer a coherence point is to Q, the higher is the corresponding ground-to-volume ratio μ.
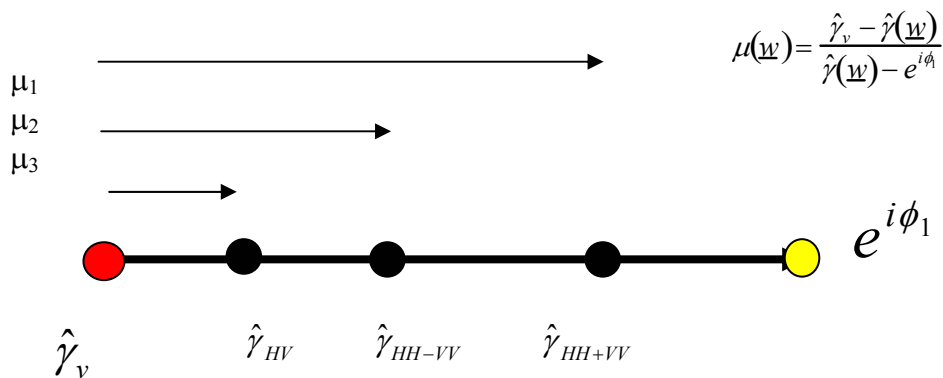

Figure 6: Relative location of polarisation states along the coherence line

While HH+VV and HH-VV can change relative position depending on whether direct ground or dihedral effects are dominant, it is very unlikely that the strongest ground-to-volume component will arise in the HV channel. This is based on scattering physics, which indicates that dihedral effects in vegetation generally lie orthogonal to HV [26], direct ground backscatter at L band has only a weak HV signal while canopy scattering has a strong HV signal. Hence it is reasonable to expect that the HV coherence channel will be ranked furthest away in distance from the true ground phase point Q (see figure 2 for experimental validation). Again some care is required, as statistical fluctuations can change the rank order and so statistical significance tests are again required.

Nevertheless, this gives us a systematic way of breaking the symmetry between the two points ψ_1, ψ_2 of deciding on the likely ground phase point and of applying the appropriate inversion model (random volume plus ground or oriented volume for example). Using this procedure we can now select the appropriate model and generate an interferogram, the phase of which, ϕ, corresponds directly to the true ground topography estimate. Note that this can be achieved through a combination of line fitting and rank ordering of coherence, both of which are fast processes to compute. As an alternative strategy to bias removal, the two points can initially be kept and each used in a stage 3 height estimation procedure (see below). As long as the tree height is less than the π height of the interferometer, then only one point will yield a good model fit thus enabling bias removal to be undertaken in stage 3. This provides a better quantitative approach but incurs the extra overhead of having to solve the model twice instead of only once for each point.

Stage 3 : Height and Extinction estimation

To estimate the two remaining parameters, height and extinction, we use the estimate of ground phase ϕ together with equation 8 to find the intersection point between the coherence line and the curve corresponding to the height/extinction variations. Figure 7 demonstrates the geometry of this intersection process. The ground phase in this simulation lies at zero degrees and we show 3 simulated coherence values along the line. By fixing σ at two different values and then varying the height, we obtain two coherence loci as shown. Where the curve intersects the line we have a candidate γ_ϖ point.
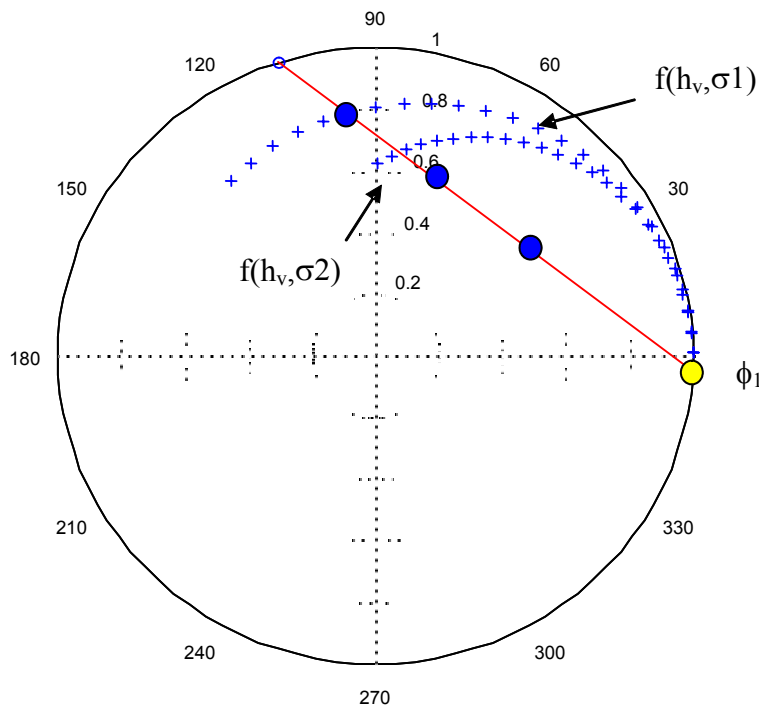

Figure 7: Geometrical interpretation of height and extinction estimation

We show two such intersections, one of which crosses the line to split the observed coherence values. This cannot be a physical solution, as it generates negative μ, which from equation 6 is not possible. We must therefore take as the first candidate solution, parameters which cause the curve to intersect the line at the *observed* coherence value furthest from ϕ (upper curve in figure 7). This ensures non-negative ground scattering components for all *observed* polarizations but makes the assumption that for the intersection coherence point, the ground-to-volume scattering ratio μ is zero. This point then becomes our estimate of γ_ϖ. Hence unambiguous height/extinction estimation with single baseline polarimetric interferometry requires that γ_ϖ be observed in the data. The robustness of the height inversion process then rests on this assumption. The basic problem arises because all intersection points beyond the furthest coherence are also valid solutions for the volume coherence (figure 8). They represent height/extinction combinations that yield a volume coherence which both satisfies the model of equation 5 and the observed data. Note however that γ_ϖ must itself lie on the line and hence the ambiguous solutions are also constrained to this line. This is an important observation, as from figure 6 the multiple solutions represent monotonically increasing ground contribution with distance along the line (figure 8).
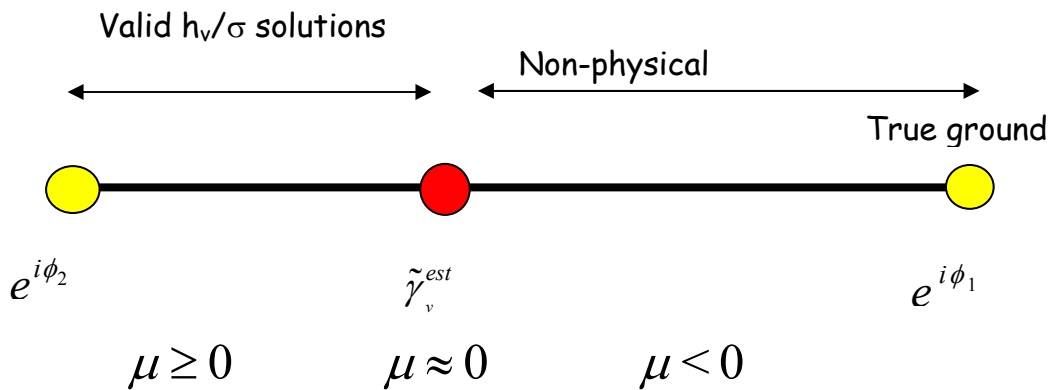

Figure 8: Line model ambiguity region

This permits us to regularize the solution by making assumptions about the minimum ground-to-volume ratio in the data. This ambiguity region has also been noted in [15,19] although in [19] a different regularization approach was employed. Note that since we know the phase point ϕ from stage 2, we can easily locate the furthest coherence point in the data. This becomes our estimate of the volume coherence $\hat{\gamma}_{est}$. From the baseline data we can estimate k_z and then pre-calculate a look-up table (LUT) of γ_ϖ as a function of h_v and σ using equation 8. By comparing $\hat{\gamma}_{est}e^{-i\phi}$ with the LUT, we can then secure estimates of the height and extinction without the need for iterative optimization algorithms. Simulations have shown that in order to secure around 10% height accuracy, the minimum ground-to-volume scattering ratio needs to be less than -10dB [27]. From the symmetry assumptions in equation 3 it follows that the HV channel will most often satisfy this requirement and hence cross polarization measurements are very important for reliable height estimation.

A.2.1 The Effect of Temporal Decorrelation on Height/Extinction estimation

We now consider how the above algorithm for height/extinction estimation must be modified in the case of repeat pass systems when temporal decorrelation becomes an important issue. Equation 10 shows that the line model is still valid and hence the line fit and ground phase estimation procedures are unchanged. However, the effect of temporal decorrelation is to make the coherence amplitude too small for the observed vegetation bias ϕ_ϖ. This is shown as the dotted line in figure 9. The true volume coherence is shifted radially to the origin by the temporal decorrelation and so the geometrical effect is to rotate and stretch the line about the unit circle ground phase point as shown in figure 9.
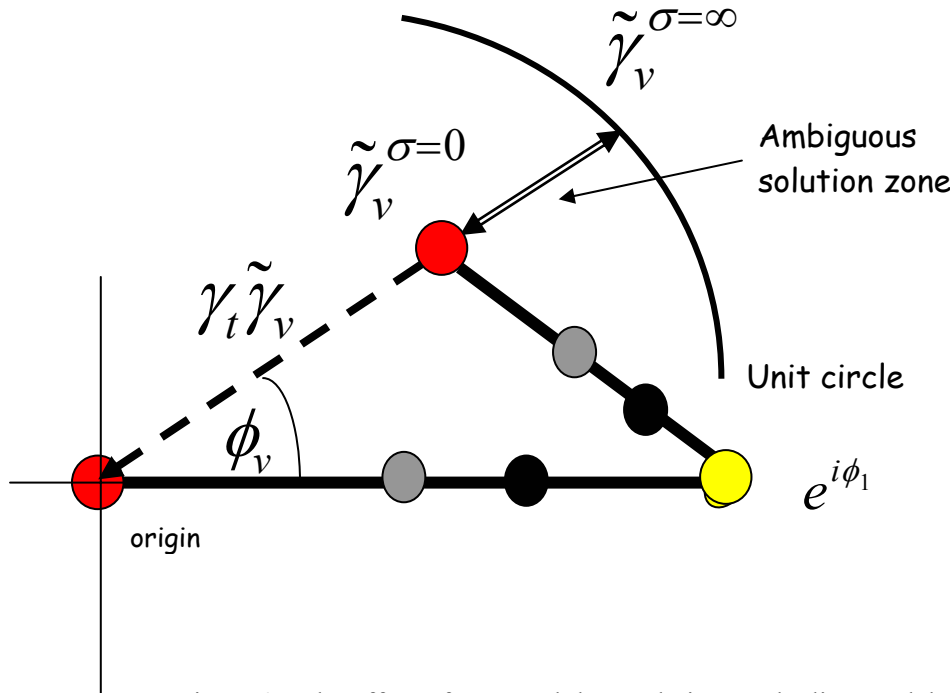
Figure 9 : The effect of temporal decorrelation on the line model

Hence there will no longer be an intersection between the height/extinction curve and the observed volume coherence point, as in figure 7. To secure a solution we must therefore move the observed volume coherence point radially in the coherence plane to compensate. The problem is we have no indication from the data itself how much temporal decorrelation has occurred. Hence the required radial scale factor is unknown. However, we can increase the coherence until we secure a first unique solution as intersection with a height/extinction curve. This will occur first for zero extinction but will then also be valid for a whole family of increasing extinction values as shown in the double line region of figure 9. This line region will extend out to the unit circle. Hence we conclude that extinction estimation becomes ambiguous in the presence of temporal decorrelation. A sensible regularization strategy is to set the extinction to zero or some other pre-determined value. In the zero extinction case, we resort to the simple sinc function model for volume coherence and the tree height is then simply related to the maximum vegetation bias ϕ_ϖ as shown in figure 9. With the sinc function model, this phase is just half the vegetation height and so the phase/height/extinction estimates in the presence of temporal decorrelation can be calculated as shown in equation 11

$$\text{temporal decorrelation} \quad \Rightarrow \quad \phi = \phi_1, \;\; h_v = \frac{2\phi_v}{k_z}, \;\; \sigma = 0 \qquad\qquad - 11)$$

A.2.2 The Effect of Vertical Tree structure on Height/Extinction estimation

So far we have assumed a uniform vertical density profile in the vegetation. However natural vegetation has significant species and age related variations in vertical structure. Figure 10 shows an example for Scots Pine trees in the Glen Affric region of Scotland [16]. Here we see tall trees with a high thin canopy. A simple way to model this structure is to add an extra phase parameter to the 2-layer model,

essentially making it a three layer structure. Figure 11 shows a schematic of this new model. The essential modification is to move the canopy away from the ground phase point and this introduces a new phase parameter ϕ_χ as shown. With this modification the line model takes the form shown in equation 12
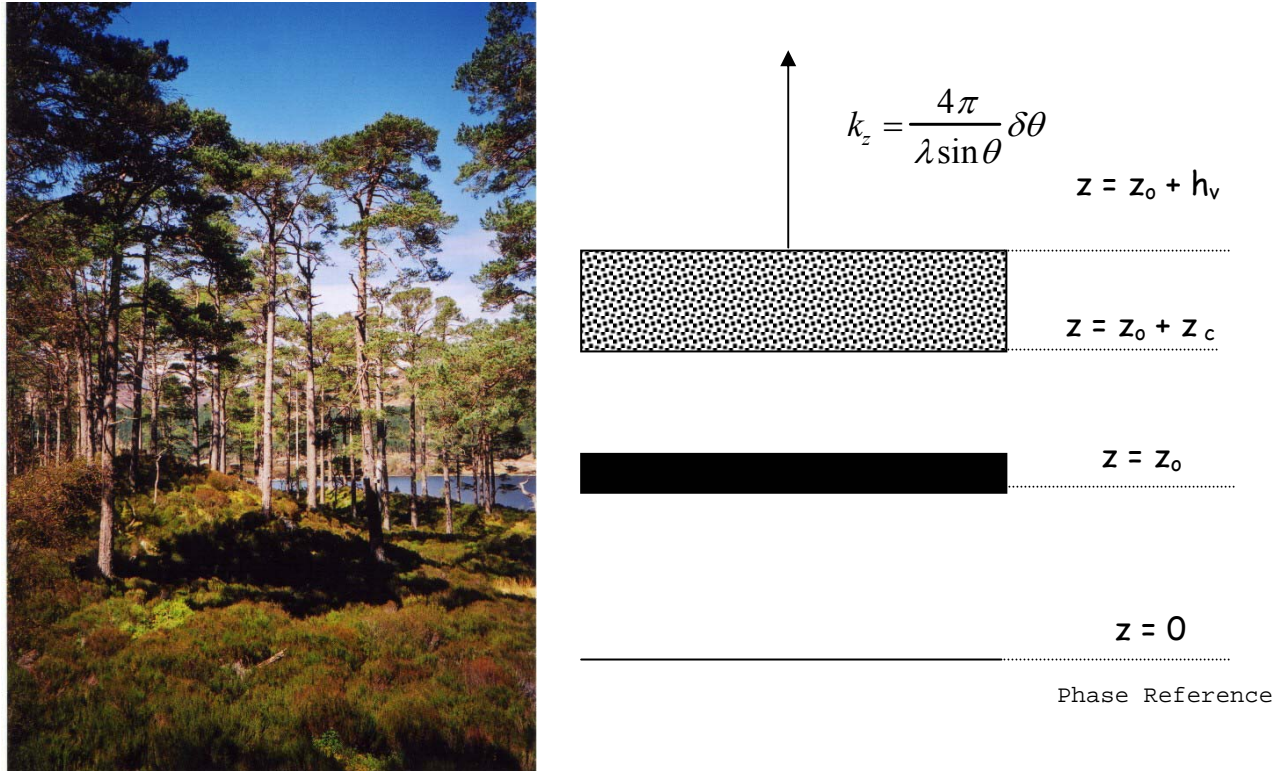

Fig. 10 Vertical tree canopy structure in natural vegetation (Scots Pine) and 3-layer modification of scattering model to account for elevated canopies

$$\tilde{\gamma} = e^{i\phi}\left(e^{i\phi_c}\tilde{\gamma}_v - \frac{\mu}{1+\mu}\left(1 - e^{i\phi_c}\tilde{\gamma}_v\right)\right) \qquad - 12)$$

Geometrically this represents a rotation of the volume coherence point about the origin. Again the line model is still valid but the observed volume coherence is now phase shifted away from its true position. Hence for a given height, the volume coherence is higher than expected based on the simple two-layer model. Nonetheless, this can be accommodated in the model by *artificially* increasing the extinction. With reference to figure 3 we can see that a fixed coherence (horizontal line) can be made to correspond to increasing tree height simply by increasing the extinction. Hence the effect of higher thinner canopies is to increase the extinction estimate with only a small error in the height. For this reason vertical structure is not too serious a limitation for SBPI if only tree height and ground topography are the important parameters of interest. The extinction however becomes an unreliable measure of tree density.

If we have vertical structure combined with temporal decorrelation then equation 11 can overestimate tree height by as much as a factor of 2. In this case only the ground topography estimation becomes a reliable parameter. However, if information is available about the canopy extent of the trees in the scene based on species or age information for example, then equation 11 can be generalized to

temporal decorrelation $+$ canopy fill F $\Rightarrow$ $\phi = \phi_1$, $h_v = \dfrac{\phi_v}{k_z(1 - \dfrac{F}{2})}$, $\sigma = 0$ $\qquad$ - 13)

where F = $(h_v - z_c)/h_v$ is the fractional canopy fill of the trees.

A.2.3 The effect of oriented structure in the volume

We have seen that for POLInSAR remote sensing applications we require there to be significant volume decorrelation. The presence of vegetation causes a loss of coherence and a phase bias. For a single layer of height hv and mean extinction σ we have shown that this coherence can be written as shown in equation 14

$$\tilde{\gamma}_v e^{i\phi(z_o)} = \frac{2\sigma e^{i\phi(z_o)}}{\cos\theta_o(e^{2\sigma h_v/\cos\theta_o} - 1)} \int_0^{h_v} e^{ik_z z'} e^{\frac{2\sigma z'}{\cos\theta_o}} dz' \qquad - 14)$$

However structured volumes, such as agricultural crops and even forests at low frequencies have different extinctions in different polarisations. Hence the volume by itself then requires characterisation by an ordered triplet of coherence values as shown in equation 15.

Equation 15 looks favourable for inversion, as it has four unknown parameters on the right and 6 observations on the left. However, by itself equation 15 is a poor predictor of coherence, as it ignores surface effects and as we have shown, the presence of the soil-air interface beneath the vegetation strongly influences the coherence

$$\sigma_V > \sigma_H \Rightarrow |\tilde{\gamma}_{VV}| > |\tilde{\gamma}_{HV}| > |\tilde{\gamma}_{HH}| \geq 0$$

$$\tilde{\gamma}_{HH} = \frac{2\sigma_H e^{i\phi(z_o)}}{\cos\theta_o(e^{2\sigma_H h_v/\cos\theta_o} - 1)} \int_0^{h_v} e^{ik_z z'} e^{\frac{2\sigma_H z'}{\cos\theta_o}} dz'$$

$$\tilde{\gamma}_{HV} = \frac{\sigma_H + \sigma_V e^{i\phi(z_o)}}{\cos\theta_o(e^{(\sigma_H + \sigma_V)h_v/\cos\theta_o} - 1)} \int_0^{h_v} e^{ik_z z'} e^{\frac{(\sigma_H + \sigma_V)z'}{\cos\theta_o}} dz' \qquad - 15)$$

$$\tilde{\gamma}_{VV} = \frac{2\sigma_V e^{i\phi(z_o)}}{\cos\theta_o(e^{2\sigma_V h_v/\cos\theta_o} - 1)} \int_0^{h_v} e^{ik_z z'} e^{\frac{2\sigma_V z'}{\cos\theta_o}} dz'$$

To progress we must use the two-layer model, but now modified to account for differential extinction. The general coherence for a vegetation+surface layer may be written as shown in equation 16

$$\tilde{\gamma}_x = e^{i\phi(z_o)} \frac{\gamma_v(k_z, \sigma_a, h_v) + \mu_x}{1 + \mu_x} \qquad -16)$$

Here μ is the ratio of surface-to-volume scattering and is generally also a function of polarisation 'x'. Hence equation 15 must be modified to a triplet of such expressions which form the oriented-volume-over-ground or 'ovog' model as shown in equation 17

$$\tilde{\gamma}_{HH} = e^{i\phi} \frac{\gamma_v(2\sigma_H, h_v) + \mu_{HH}}{1 + \mu_{HH}}$$

$$\tilde{\gamma}_{HV} = e^{i\phi} \frac{\gamma_v(\sigma_H + \sigma_V, h_v) + \mu_{HV}}{1 + \mu_{HV}}$$

$$\tilde{\gamma}_{VV} = e^{i\phi} \frac{\gamma_v(2\sigma_V, h_v) + \mu_{VV}}{1 + \mu_{VV}}$$

- 17)

This model now has 7 unknowns on the right and only 6 observations on the left. Hence in the presence of orientation effects we need to fix one parameter for inversion. There are various strategies for the inversion of equation 17 being pursued in the literature, for example we can assume that one of the μ values is zero, that the ground phase ϕ is known or as an important special case that the differential extinction is zero in which case we return to our random volume over ground model. Equation 17 has a convenient geometrical representation inside the unit circle of the complex plane. Figure 11 shows this structure. The surface phase ϕ acts as a focus for three rays, representing each of the three primary polarisation combinations. Importantly, the coherence in each polarisation channel is confined to move along its own ray, depending on the value of μ. The volume coherences (defined by μ = 0), establish a special triplet of points along the rays as shown. This geometry clearly demonstrates that the biggest error source for unknown orientation effects will be a bias in the ground phase estimate (the three points still almost form a line but intersect the unit circle in the wrong place). This in turn will lead to an underestimation in height.
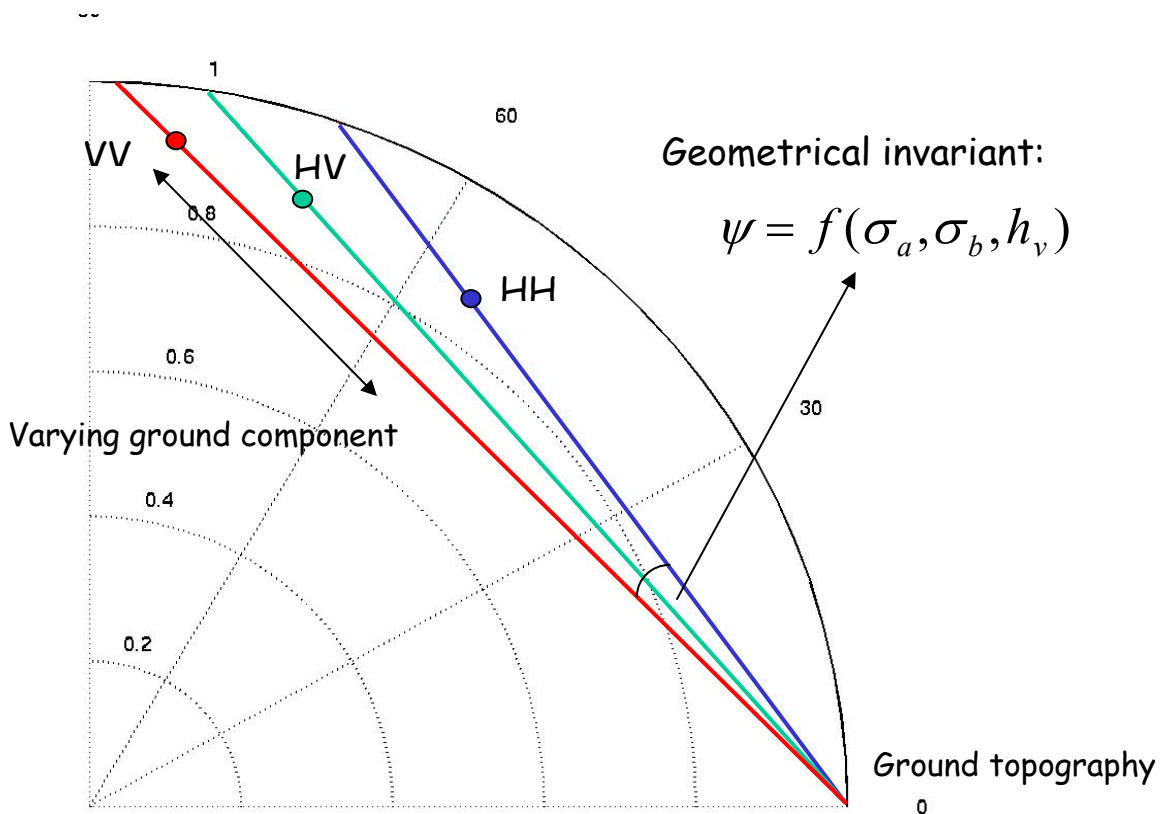

Figure 11 : The geometry of the oriented-volume-over-ground 'ovog' model

A.3. ALGORITHM ASSESSMENT USING Simulated SAR data

In previous publications, validation of these algorithms has been provided using airborne L and P band SAR data across a range of test sites [6,16,19]. These have also addressed the more practical aspects of radar data processing required for operational implementation of these algorithms. Here we concentrate on a different type of validation, involving the use of coherent electromagnetic scattering models. In order to illustrate application of the above algorithm to POLInSAR data, we employ a canopy scattering model with predetermined structure and attempt reconstruction of the height and ground topography from complex coherence data. Note that this model is not the same one used for the algorithm development. To generate a fair test of algorithm performance, a full Maxwell equation based wave propagation and scattering model is used to generate the test data. DSTL Malvern have developed such a capability to model forest scattering in detail, employing a 3-D voxel based vector wave propagation and scattering model tied to a detailed description of branch, leaf and trunk distributions [24,25]. Penetration and scattering are calculated as a function of wavelength and polarisation. The underlying surface scattering is modelled as a tilted Bragg surface and mutual interactions such as ground-trunk and canopy-ground are incorporated in the model. The technique is fully coherent and so can be used to model volume decorrelation effects in polarimetric radar interferometry. The simulated data is free from temporal decorrelation, motion or co-registration errors and SNR effects. Hence we can apply the full inversion scheme to the data as a 'best case' scenario.

The SAR simulator was initialised using a point spread function matched to the airborne DLR E-SAR system with 0.69m azimuthal and 1.38m ground range resolution. Simulations were carried out at L-band (23cm wavelength) and at 45 degrees angle of incidence from 3km altitude with 10m and 20m horizontal baselines. These parameters closely match those used for operational E-SAR trials over forest test sites.

A full random canopy (F = 1) of 10m height placed above a flat Bragg surface was chosen as the test configuration, The branches chosen to populate the random canopy had dimensions chosen from Gaussian distributions. Branch length had mean 1.5m and standard deviation 0.2m, branch radius had mean 1.5cm and standard deviation 0.2cm. Branch length distribution was truncated at 2.0m and 1.0m, and radii at 1.0cm and 2.0cm. There were 59,153 branches in the canopy with dimensions 56m by 56m by 10m, corresponding to a mean volume fraction of 0.2%. In the simulation branches are further subdivided into smaller elements depending upon the resolution cell size, so that over 200,000 elements existed in the simulation.

Figure 12 shows simulated SAR images of the canopy scene. Note that the canopy scattering appears in all polarization channels, including the cross-polar channel HV. The surface scattering has zero cross polarization but has different scattering components in HH and VV as consistent with the Bragg model. From analysis of the model, the ground contributions beneath the canopy are attenuated by a (one-way) mean extinction of 0.28 dB/m.

We concentrate on a linear azimuth transect through the data as shown. Figure 13 shows sample coherence loci for the point P. Coherence was estimated using a 60-look local boxcar average. In 13 a) we show the interferometric coherence loci for a 10m baseline. Also shown are the least square line fits through the data points. The true ground phase is 0 degrees and we clearly see the vegetation bias in all polarization channels. Note how the line model is a good fit and the intersection point lies close to the true ground phase. In 13 b) we show, for the same test point P, the 20m baseline data for comparison. Here we see a decrease in coherence due to the larger baseline but note that the line fit is still good and unit circle intersect remains close to the true value. Note however the increased variance of coherence estimates, in agreement with equation 9.

In both plots, the HV channel is identified by a circle symbol and we see it has the largest bias as expected from the 2-layer model. We show 5 polarisation states in all, HH, VV, HV, HH+VV and HH-VV. Note that by simply using the phase difference between polarizations we would seriously underestimate the true height. As an example figure 14 shows the estimated height obtained from the phase difference between HH and HV interferometric channels. We see that the average estimate is around 2.5m, well below the true value of 10m. Hence model based corrections are required to obtain better estimates of height. Here we apply the 2-layer model via the geometrical inversion procedure developed above. Figure 15 shows the output from the

3-stage inversion model. Here we show the combined tree height and ground topography estimation for the azimuth transect. We see much improved height estimation and the removal of vegetation bias from the topography estimate.
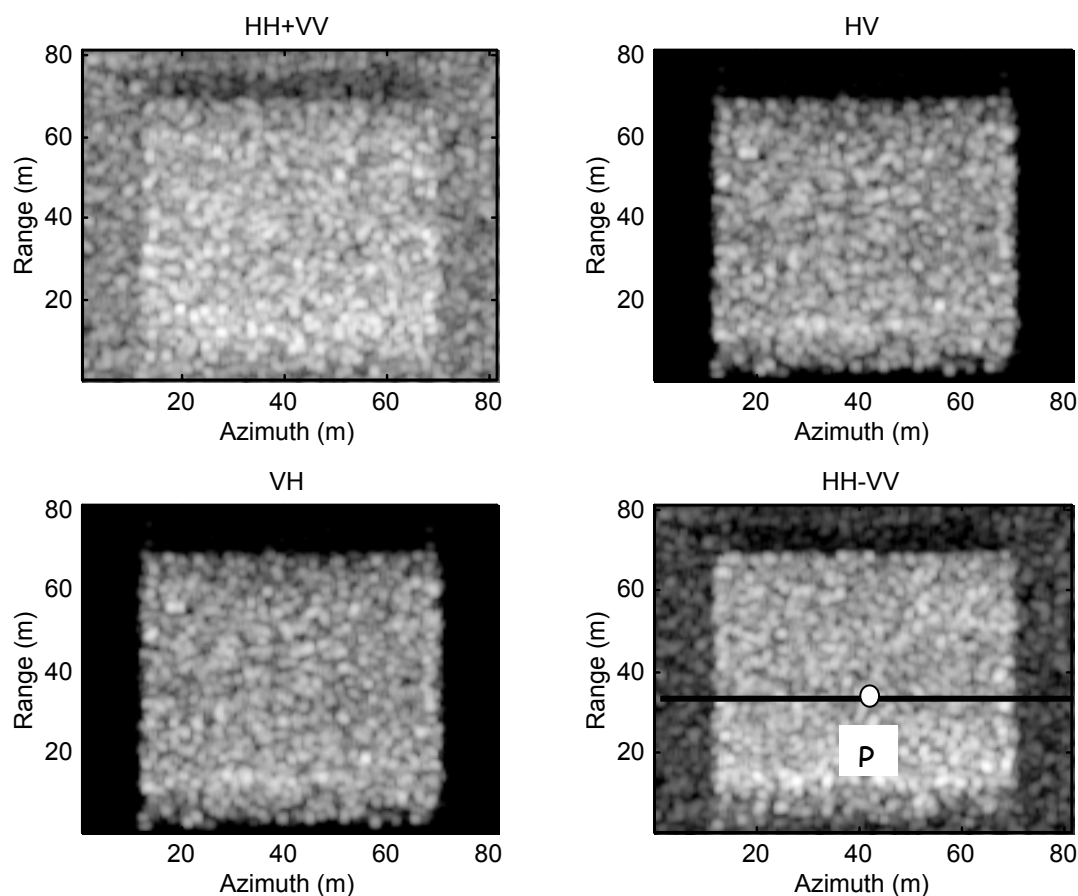

Figure 12 : Simulated L-band SAR images of 10m canopy

Note how the estimates are poor at the edges of the stand, This arises because of the boxcar averaging employed, mixing surface and volume scattering. This causes the local coherence estimates to be low which leads locally to poor parameter estimates. Adaptive edge filtering techniques are being investigated to help resolve this problem [23].

A.4. Conclusions

In this section we have developed a simplified 3-stage inversion method for the estimation of underlying ground topography, vegetation height and mean extinction from single baseline polarimetric interferometric SAR data. We have highlighted key potential sources of error in the inversion procedure and shown that to secure good estimates we require one main assumption, namely that in *one* (not all) of the observed polarization channels, the ground-to-volume scattering ratio is small (less than −10dB to secure 10% height accuracy). This highlights the importance of measuring the HV cross-polarized channel for accurate height estimation.

A second key issue is the length of the visible line inside the coherence unit circle. If the line length becomes too short then the inversion becomes unstable. This can arise at very high frequencies, where extinction by vegetation dominates the variation of ground scattering with polarization. However, as long as the visible line length is greater than the complex coherence fluctuations, the line model can be easily extrapolated to

find the ground phase point. Hence the technique is inherently robust against the presence or absence of ground-trunk dihedral effects and/or topographic variation. Consequently it can still provide parameter estimates, even in difficult terrain such as forested slopes where the dihedral return can be attenuated due to topographic variations.

The issue of line visibility can also be used to examine the frequency dependence of the inversion process. Extinction generally increases with frequency and so the line visibility can be expected to decrease as wavelength decreases. However, at very low frequencies the propagation itself can become anisotropic (a function of polarization). In this case the line model is no longer valid, leading to a consequent decrease in parameter accuracy. For these reasons most of our studies have been centred on L-band as a good compromise between the two extremes and because of its well developed technology for air and space borne deployment. However, some initial studies have shown that the technique also applies at P-band for tropical forest environments [19].

We have further considered the effects of temporal decorrelation, vertical structure and volume orientation on errors in SBPI inversion and have shown that in the presence of temporal effects, extinction estimation becomes ambiguous and resort must be made to phase difference algorithms with structure related correction parameters. The effect of vertical structure such as an elevated canopy is to impose a phase transformation on the volume coherence term. This is compensated in the 2-layer model by artificially increasing the extinction. Finally, the effect of orientation in the volume is to split the coherence loci into a fan of three lines centred on the true ground phase. If uncompensated this leads to bias in the ground phase estimate and underestimation of height. Coherent SAR simulations using the DSTL vector wave scattering model have been used to illustrate the algorithms and demonstrate the need to employ such model based corrections to interferometric phase in order to achieve precision vegetation parameter retrieval. These results clearly demonstrate that tree height and underlying ground topography can be retrieved from a single frequency, single baseline polarimetric sensor. This leads to the possibility of mapping these parameters using air or space borne sensors on regional or even global scales. This is especially important given the close relationship between tree height and biomass [28,29].
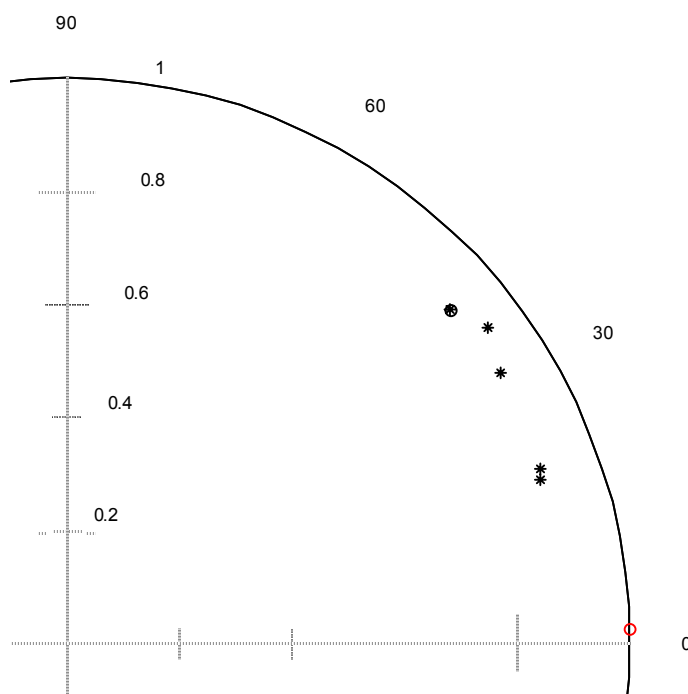

Figure 13 a : Sample coherence loci for the point P in figure 12a, 10m baseline
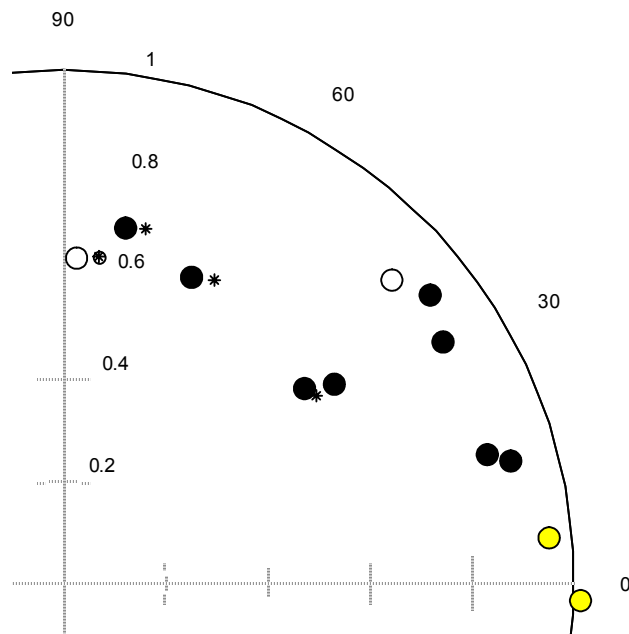
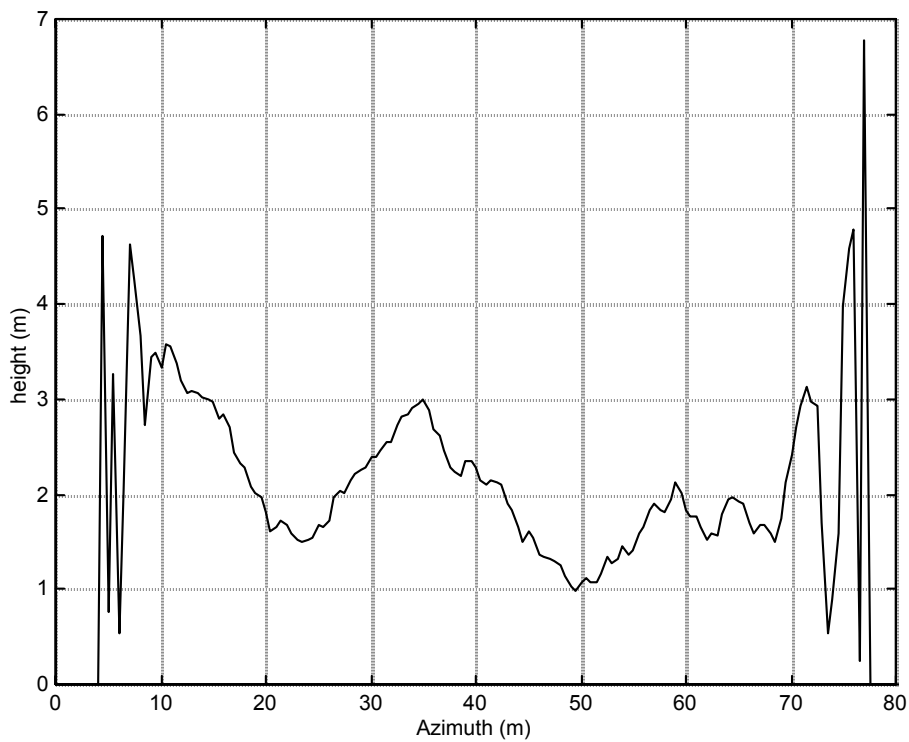Figure 13 b : Sample coherence loci for the point P in figure 12a 20m baseline

Figure 14 a : Tree height estimation based on phase difference between HH and HV interferometric channels
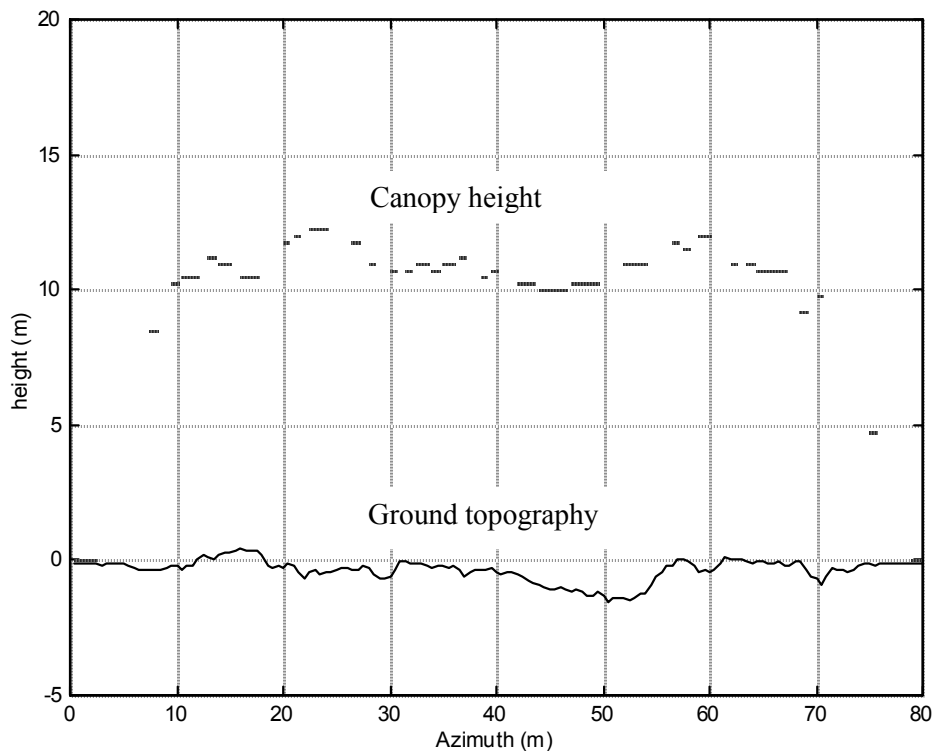
Figure 14 b : Tree height estimation based on 3 –stage model inversion

A.5. REFERENCES

[1] CLOUDE S. R., PAPATHANASSIOU K.P., "Polarimetric Optimisation in Radar Interferometry", *Electronics Letters*, Vol. 33, N0. 13, June 1997, pp. 1176-1178

[2] CLOUDE S. R., PAPATHANASSIOU K.P, "Polarimetric SAR Interferometry", *IEEE Transactions Geoscience and Remote Sensing*., Vol. GRS-36. No. 5, September 1998, pp. 1551-1565

[3] TREUHAFT R. N.,MADSEN S., MOGHADDAM M., VAN ZYL J.J.,"Vegetation Characteristics and Underlying Topography from Interferometric Data",*Radio Science*, Vol. 31, Dec, 1996, pp. 1449-1495

[4] TREUHAFT R.N., SIQUERIA P., "Vertical Structure of Vegetated Land Surfaces from Interferometric and Polarimetric Radar", *Radio Science*, Vol. 35(1), January 2000, pp 141-177

[5] LEE J.S.,HOPPEL K.W., MANGO S.A., MILLER A., "Intensity and Phase Statistics of Multi-Look Polarimetric and Interferometric SAR Imagery", *IEEE Transactions Geoscience and Remote Sensing.* GE-32, 1994, pp. 1017-1028

[6] PAPATHANASSIOU K.P., CLOUDE S. R., "Single Baseline Polarimetric SAR Interferometry", *IEEE Transactions Geoscience and Remote Sensing*, Vol 39/11, November 2001, pp 2352-2363

[7] REIGBER A., MOREIRA A., "First Demonstration of Airborne SAR Tomography Using Multi-Baseline LBand Data", *IEEE Transactions on Geoscience and Remote Sensing*, Vol. 38/5, September 2000, pp 2142-2152

[8] REIGBER A., "Airborne Polarimetric SAR Tomography", DLR report ISRN DLR-FB-2002-02, 2002

[9] VAN ZYL J.J., KIM Y, "The Relationship between Radar Polarimetric and Interferometric Phase", CD Proceedings of IEEE-IGARSS 2000, Hawaii, USA

[10] TREUHAFT R.N., CLOUDE, S.R., "The Structure of Oriented Vegetation from Polarimetric Interferometry", *IEEE Transactions Geoscience and Remote Sensing*, Vol. 37/2, No. 5, September 1999, pp 2620-2624

[11] CLOUDE S. R., PAPATHANASSIOU K.P,BOERNER W.M., "The Remote Sensing of Oriented Volume Scattering Using Polarimetric Radar Interferometry", Proceedings of ISAP 2000, Fukuoka, Japan, August 2000, pp 549-552

[12] SEYMOUR S., CUMMING I.G., "Maximum Likelihood Estimation for SAR Interferometry", Proceedings of IEEE-IGARSS'94, Pasadena, USA

[13] TOUZI R, LOPES A., BRUNIQUEL J, VACHON P.W., "Coherence Estimation for SAR Imagery", *IEEE Transactions Geoscience and Remote Sensing,* VOL. GRS-37, Jan 1999, pp 135-149

[14] ISOLA M., CLOUDE, S.R., "Forest Height Mapping using Space Borne Polarimetric SAR Interferometry", CD Proceedings of IEEE International Geoscience and Remote Sensing Symposium (IGARSS 2001), Sydney, Australia, July 2001

[15] TABB M., CARANDE R., "Robust Inversion of Vegetation Structure Parameters from Low-Frequency, Polarimetric Interferometric SAR", CD Proceedings of IEEE-IGARSS 2001, Sydney Australia

[16] CLOUDE S.R., WOODHOUSE I.H., HOPE J., SUAREZ-MINGUEZ J.C., OSBORNE P., WRIGHT G., "The Glen Affric Radar Project: Forest Mapping using dual baseline polarimetric radar interferometry", Proceedings of Symposium on "Retrieval of Bio and Geophysical Parameters from SAR for Land Applications", University of Sheffield, England, September 11-14, 2001, ESA publication SP-475, pp 333-338

[17] ULBRICHT A., FABREGAS X., SAGUES L., ``Applying Polarimetric Interferometric Methods to Invert Vegetation Parameters from SAR Data'', CD Proceedings of the IEEE International Geoscience and Remote Sensing Symposium (IGARSS), 9-13 July, Sydney, Australia, 2001

[18] ULBRICHT A., FRABREGAS X., CASAL M., ``Experimental and Theoretical Aspects of Inversion of Polarimetric Interferometric Data'', Proceedings of the Open Symposium on Propagation and Remote Sensing, URSI, Commission F, 12-15 February, Garmisch-Partenkirchen, Germany, 2002

[19] BRANDFASS M., HOFMANN C., MURA J.C., MOREIRA J., PAPATHANASSIOU K.P., ``Parameter estimation of Rain Forest Vegetation via Polarimetric Radar Interferometric Data'', Proceedings of SPIE 2001, Toulouse, France, August 2001

[20] FLYNN T., TABB M., CARANDE R., "Coherence region Shape Estimation for Vegetation Parameter Estimation in POLINSAR", Proceedings of IGARSS 2002, Toronto, Canada, pp V 2596-2598

[21] TABB M., FLYNN T., CARANDE R., "Direct Estimation of Vegetation Parameters from Covariance Data in POLINSAR", Proceedings of IGARSS 2002, Toronto, Canada, pp III 1908-1910

[22] YAMADA H., SATO K., YAMAGUCHI Y., BOERNER W.M. "Interferometric Phase and Coherence of Forest Estimated by ESPRIT based POLINSAR", Proceedings of IGARSS 2002, Toronto, Canada, pp II 832-834

[23] LEE J.S., CLOUDE S.R., PAPATHANASSIOU K.P., GRUNES M.R., AINSWORTH T., " Speckle Filtering of POLINSAR Data", Proceedings of IGARSS 2002, Toronto, Canada, pp II 829-831

[24] WILLIAMS M. L.,"Simulating Low Frequency SAR Clutter from a Pine Forest", Proeedings of 3rd European SAR Conference (EUSAR), 23-25 May, 2000, Munich, Germany, pp 149-152

[25] WILLIAMS M.L., "Prediction and Observation of SAR Clutter from Vegetation Canopies", Proceedings of IGARSS '99, Hamburg, Germany, pp 1983-1985

[26] FREEMAN A., DURDEN S.L., "A Three Component Model for Polarimetric SAR Data", *IEEE Transactions on Geoscience and Remote Sensing*, Vol. GE-36, 1998, pp. 963-973

[27] PAPATHANASSIOU K.P., HAJNSEK I., MOREIRA A., CLOUDE S.R., ''Forest Parameter Estimation using a Passive Polarimetric Micro-Satellite Concept'', Proceedings of European Conference on Synthetic Aperture Radar, EUSAR'02, pp. 357-360, Cologne, Germany, 4-6 June 2002.

[28] METTE T., PAPATHANASSIOU K.P., HAJNSEK I., and ZIMMERMANN R., ''Forest Biomass Estimation using Polarimetric SAR Interferometry'', Proceedings IGARSS'02 (CD-ROM), Toronto, Canada, 22-26 June 2002

[29] PAPATHANASSIOU K.P., METTE T., HAJNSEK I, KRIEGER G. and MOREIRA A., ''A Passive Polarimetric Micro-Satellite Concept for Global Biomass Mapping', Proceedings of the PI-SAR Workshop (CD-ROM), Tokyo, Japan, 29-30 August 2002

Appendix B: POLInSAR in target detection Applications

In this section we consider the problem of radar detection of stationary targets obscured by foliage clutter. This is a classical detection problem for which the usual solution approach is to reduce the radar centre frequency as far as possible, so minimising scattering by the foliage while hopefully maintaining a significant target response. These approaches are based on backscatter intensity as the prime radar observable. In this paper we consider a new approach. Here we employ the phase of a radar interferometer as the prime observable and attempt the detection of targets by using the variation of phase with polarisation to reduce the foliage returns and maintain the target response. In section 2 we provide an introduction to polarimetric radar interferometry and consider the nature of the phase signal obtained in volume scattering. In section 3 we then extend this argument to consider the influence of a target on the observed phase and show how we can use this to develop a filter for enhanced target detection. In section 4 we describe a processing algorithm based on this analysis of volume scattering and in section 5 summarise the main components of a vector wave propagation and scattering model used to simulate coherent radar returns from targets embedded in foliage. In section 6 we present results from a simulation based on this model of corner reflectors embedded in a pine forest and demonstrate the ability of this technique to provide enhanced detection by showing raw and filtered signal channels for a cluster of hidden trihedral reflectors.

B.1. Polarimetric Interferometric SAR (POLInSAR)

The techniques considered in this paper employ imaging radar interferometry, a dual sensor technology which coherently combines backscatter measurements from two ends of a baseline B, shown as positions 1 and 2 in figure 1 (see [1] for a general review and extensive background references). The sensors are assumed to move in parallel linear trajectories in the x-direction. This enables generation of a synthetic aperture for both sensors and hence high resolution imaging in the range/azimuth or x,z' plane. By co-registering these two images we can then form the phase difference and obtain a high resolution 2-D image of the variation of interferometric phase in the x,z' plane. The measurements can either be made by a single platform dual antenna system (single-pass) or by repeat visits of a single antenna system (repeat-pass). The latter suffers from loss of signal coherence due to any temporal changes in the scene between passes. In this paper we ignore such temporal decorrelation effects and concentrate instead on the influence of combined surface and volume scattering.

Although interferometry requires the backscatter amplitude to be sufficiently above the system noise level, the key observable of interest is not amplitude but the interferometric phase. This is non-zero due to the slightly different propagation path lengths, Δr, from sensors 1 and 2 to a point on the surface. From the geometry in figure 1and by assuming we both transmit and receive from points 1 and 2, this phase has the form shown in equation 1 (see [1] for a full derivation).

$$\exp(i2k\Delta r) \approx \exp(i\frac{4\pi\Delta\theta}{\lambda}y') \approx \exp(i\frac{4\pi B_n}{\lambda R}y') \qquad\text{- 1)}$$

where $\Delta\theta \approx Bn/R$ if $R >> B$ and the co-ordinate y' is defined as normal to the slant range direction such that y',z' define a local orthogonal co-ordinate system as shown in figure 1. Note that the interferometric sensitivity depends only on the normal component of the baseline, B_n, which depends on the absolute baseline B, the baseline orientation angle δ and the angle of incidence θ_o as defined in figure 1. Transforming to the surface y,z co-ordinates using the local angle of incidence θ we can also express equation 1 in the modified form $\exp(i\,\phi(y, z))$ as shown in equation 2

$$\phi(\mathrm{y}, z) = \mathrm{y}\left(\frac{2kB_n\cos\theta}{R} - 2\Delta k\sin\theta\right) + z\left(\frac{2kB_n\sin\theta}{R} + 2\Delta k\cos\theta\right) \quad \Delta k = \frac{kB_n}{R\tan\theta} \qquad\text{- 2)}$$

Here we have further included the possibility of making a wavenumber shift Δk between the two images [2]. As is apparent from equation 2, we can then always remove the 'y' dependence of the phase ϕ by choosing Δk based on the geometry of the system. In this case the interferometric phase depends only on the height of the scatterer above the reference plane (the z co-ordinate in figure 1). To study any decorrelation in the 'z' direction, we then define an effective propagation constant using 1 and 2, as shown in equation 3

$$k_z = \frac{4\pi\Delta\theta}{\lambda\sin\theta} \approx \frac{4\pi B_n}{\lambda R\sin\theta}$$

- 3)

In foliage examples there will be a random distribution of scatterers in the vertical direction. This causes fluctuations in the phase that are manifest as a drop in the interferometric coherence γ [1]. In polarimetric systems we have 3 channels of complex data at positions 1 and 2 characterised by the elements of the coherent scattering matrix S_{HH}, S_{VV} and S_{HV} [3,4]. In this case the fluctuations can be characterised by a 6 x 6 Hermitian coherency matrix $[\Theta]$ as defined in equation 4 [3]. To generate the appropriate coherence we need first to project the channels onto a 3 dimensional complex unitary weight vector w_1 to generate a complex scalar s_1 as shown in equation 5. Similarly we can define a different weight vector w_2 and scalar s_2 at position 2. The unitary weight vectors can be parameterised in the form shown in equation 5. Here α is the selected scattering mechanism and β the orientation of that mechanism in the plane of polarisation. Further details of the relationship between w and polarisation parameters can be found in [3,4]. The interferometric coherence for arbitrary polarisation is then defined as the average normalised product of the scalar projections as shown in equation 5 [3]
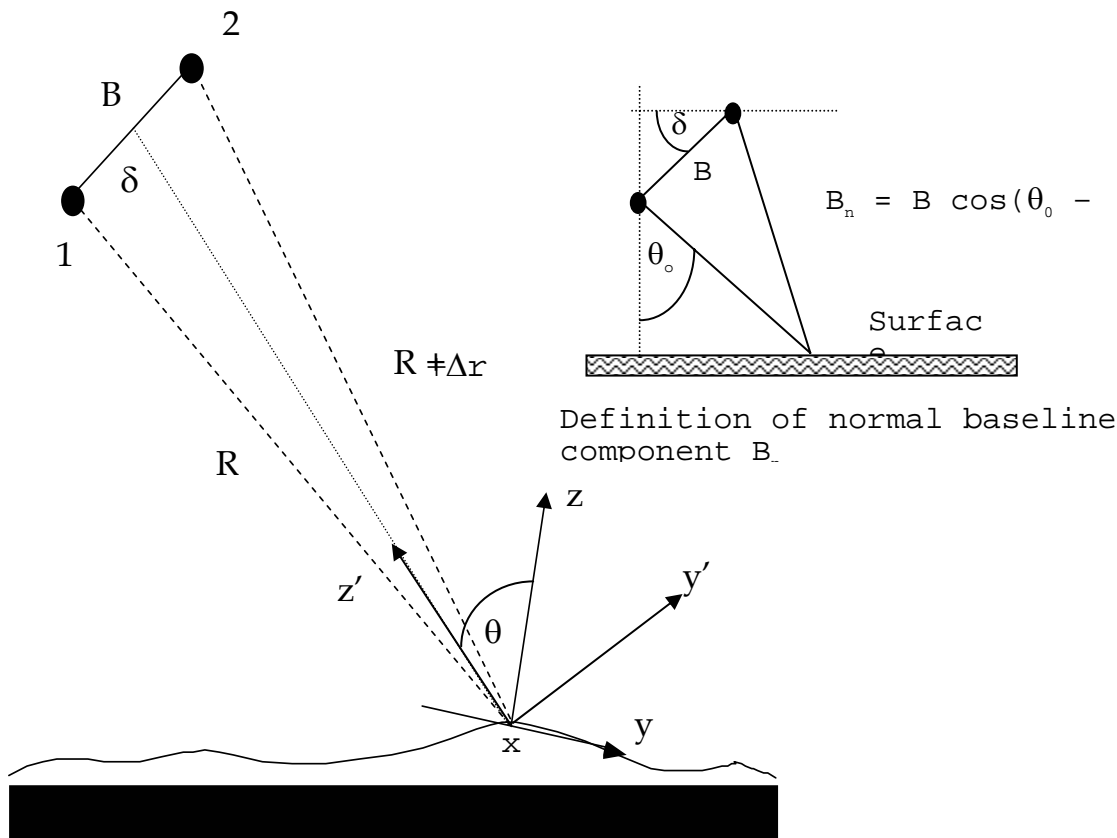

Figure 1: Radar interferometry and surface geometry.

$$[\Theta] = \left\langle \begin{bmatrix} \underline{k}_1 \\ \underline{k}_2 \end{bmatrix} \begin{bmatrix} \underline{k}_1^{*T} & \underline{k}_2^{*T} \end{bmatrix} \right\rangle = \left\{ \begin{array}{c} \begin{bmatrix} [T_{11}] & [\Omega_{12}] \\ [\Omega_{12}]^{*T} & [T_{22}] \end{bmatrix} \quad \underline{k} = \frac{1}{\sqrt{2}} \begin{bmatrix} S_{HH} + S_{VV} \\ S_{HH} - S_{VV} \\ 2S_{HV} \end{bmatrix} \\[40pt] \begin{bmatrix} [C_{11}] & [\Gamma_{12}] \\ [\Gamma_{12}]^{*T} & [C_{22}] \end{bmatrix} \quad \underline{k} = \begin{bmatrix} S_{HH} \\ \sqrt{2} S_{HV} \\ S_{VV} \end{bmatrix} \end{array} \right.$$

- 4)

Note that the coherence amplitude and phase can be combined and represented as a point inside the unit circle of the complex plane. We see that the coherence and phase can be expressed in terms of 3x3 block elements of the 6 x 6 matrix [Θ]. In equation 4 we have shown two different representations of [Θ] [4]. The coherency form is generated by a Pauli matrix expansion of the symmetric 2 x 2 complex scattering amplitude matrix [S]. This leads to a polarimetric coherency matrix [T] as shown in 5. The covariance matrix [C] follows from a straightforward vectorial expansion of [S]. The two are unitarily equivalent [4] and so have the same eigenvalues but different eigenvectors. We shall make use of both representations in this paper. To evaluate this coherence we now need to estimate the block 3x3 matrices [T] and [Ω].

$$\underline{w} = \begin{vmatrix} \cos\alpha\, e^{i\psi_1} \\ \sin\alpha\cos\beta\, e^{i\psi_2} \\ \sin\alpha\sin\beta\, e^{i\psi_3} \end{vmatrix} \qquad \begin{array}{l} 0 \leq \alpha \leq \dfrac{\pi}{2} \\[8pt] -\pi < \beta \leq \pi \end{array} \qquad \Rightarrow$$

$$\left. \begin{array}{l} s_1 = \underline{w}_1^{*T} \underline{k}_1 \\ s_2 = \underline{w}_2^{*T} \underline{k}_2 \end{array} \right\} \Rightarrow \left\{ \begin{array}{c} \gamma = \dfrac{\left| \langle s_1 s_2^* \rangle \right|}{\sqrt{\langle s_1 s_1^* \rangle \cdot \langle s_2 s_2^* \rangle}} \; = \dfrac{\left| \underline{w}_1^{*T} \Omega_{12} \underline{w}_2 \right|}{\sqrt{\underline{w}_1^{*T} T_{11} \underline{w}_1 \cdot \underline{w}_2^{*T} T_{22} \underline{w}_2}} \\[20pt] \phi = \arg(\langle s_1 s_2 * \rangle) = \arg\left(\underline{w}_1^{*T} \Omega_{12} \underline{w}_2 \right) \end{array} \right.$$

- 5)

B.1.1 The Coherence of Volume Scattering

In many vegetation problems, the scatterers in a volume will have some residual orientation correlation due to their natural structure (branches in a tree canopy for example). In this case wave propagation through the volume is characterised by two eigenpolarisations a and b (which we assume are unknown but orthogonal linear polarisations). Only along these eigenpolarisations is the propagation simple, in the sense that the polarisation state does not change with depth into the volume [5]. By assuming that the medium has reflection symmetry about the (unknown) axis of its eigenpolarisations, we obtain a polarimetric coherency matrix [T] and corresponding covariance matrix [C] in the a,b basis for backscatter from the volume as shown in equation 6 [4]

$$[T] = \begin{vmatrix} t_{11} & t_{12} & 0 \\ t_{12}^* & t_{22} & 0 \\ 0 & 0 & t_{33} \end{vmatrix} \qquad [C] = \begin{vmatrix} c_{11} & 0 & c_{13} \\ 0 & c_{22} & 0 \\ c_{13}^* & 0 & c_{33} \end{vmatrix}$$

- 6)

We can now obtain an expression for the matrices $[T_{11}]$ and $[\Omega_{12}]$ for an oriented volume extending from $z = z_0$ to $z = z_0 + h_v$ as vector volume integrals as shown in equations 7 and 8 [5,6]

$$[\Omega_{12}] = e^{i\phi(z_o)} R(2\beta) \left\{ \int_0^{h_v} e^{ik_z z'} e^{\frac{(\sigma_a + \sigma_b)z'}{\cos\theta_o}} P(\tau) \, T \, P(\tau^*) dz' \right\} R(-2\beta) \qquad - 7)$$

$$[T_{11}] = R(2\beta) \left\{ \int_0^{h_v} e^{\frac{(\sigma_a + \sigma_b)z'}{\cos\theta_o}} P(\tau) \, T \, P(\tau^*) dz' \right\} R(-2\beta) \qquad - 8)$$

where for clarity we have dropped the brackets around matrices inside the integrals and defined the following terms

$$R(\beta) = \begin{bmatrix} 1 & 0 & 0 \\ 0 & \cos\beta & \sin\beta \\ 0 & -\sin\beta & \cos\beta \end{bmatrix} \qquad - 9)$$

$$P(\tau) \, T \, P(\tau^*) = \begin{bmatrix} \cosh\tau & \sinh\tau & 0 \\ \sinh\tau & \cosh\tau & 0 \\ 0 & 0 & 1 \end{bmatrix} \begin{bmatrix} t_{11} & t_{12} & 0 \\ t_{12}^* & t_{22} & 0 \\ 0 & 0 & t_{33} \end{bmatrix} \begin{bmatrix} \cosh\tau^* & \sinh\tau^* & 0 \\ \sinh\tau^* & \cosh\tau^* & 0 \\ 0 & 0 & 1 \end{bmatrix} \qquad - 10)$$

$$\tau = \left(\frac{\sigma_a - \sigma_b}{2} + ik(\chi_a - \chi_b) \right) \frac{z'}{\cos\theta_o} \qquad - 11)$$

Here R is a rotation matrix to allow for mismatch between the radar co-ordinates and the projection of the eigenstates into the polarisation plane. P is a 3 x 3 differential propagation matrix accounting for differential phase (birefringence) and attenuation (dichroism) in the medium via the complex differential propagation constant τ. The waves propagate with extinction σ where $\sigma_a \geq \sigma_b$ and refractivities (1-index of refraction) χ [5].This now enables us to generate the coherence for any choice of weight vector w in equation 5. However we are primarily interested in the variability of coherence with changes in w and so employ the coherence optimiser developed in [3], which requires solution of an eigenvalue problem as shown in equation 12.

$$\left. \begin{aligned} [T_{22}^{-1}] [\Omega_{12}]^{*T} [T_{11}^{-1}] [\Omega_{12}] \, \underline{w}_2 &= \lambda \underline{w}_2 \\ [T_{11}^{-1}] [\Omega_{12}] [T_{22}^{-1}] [\Omega_{12}]^{*T} \underline{w}_1 &= \lambda \underline{w}_1 \end{aligned} \right\} \quad 0 \leq \lambda = \gamma_{opt}^2 \leq 1 \qquad - 12)$$

The eigenvalues of these matrices are all real positive and indicate the variability of coherence with polarisation. For example, if the three eigenvalues are equal then the coherence is invariant to polarisation. As the eigenvalues are invariant to unitary transformations of the vector k we can replace [T] by [C] and [Ω] by [Γ] in equation 12. This is important because to account for the effects of propagation on the polarimetric response of an oriented volume, it is simpler to employ the covariance [C] in the a,b basis rather than the coherency matrix [T]. We can then calculate the 3 complex optimum coherence values such that $1 \geq |\tilde{\gamma}_1| \geq |\tilde{\gamma}_2| \geq |\tilde{\gamma}_3| \geq 0$ as shown in equation 13 (see [6] for details). The key steps involved are to first convert from [T] to [C] in 12, assume that $[C_{11}] = [C_{22}]$ and then show that $[C_{11}]^{-1} [\Gamma_{12}]$ is diagonal in the a,b basis using the analytic expressions in equations 6,7 and 8. The inverse matrix can be easily calculated as a 2 x 2 sub-matrix from the symmetry constraint of equation 6. This then confirms that the maximum coherence

is always obtained in the a,b basis and evaluation of the corresponding eigenvalues in equation 12 leads to the following expressions for the ranked coherence optima.

$$1 \geq \left|\widetilde{\gamma}_1\right| \geq \left|\widetilde{\gamma}_2\right| \geq \left|\widetilde{\gamma}_3\right| \geq 0$$

$$\widetilde{\gamma}_1 = f(\sigma_a) = \frac{2\sigma_a \, e^{i\phi(z_o)}}{\cos\theta_o (e^{2\sigma_a h_v / \cos\theta_o} - 1)} \int_0^{h_v} e^{ik_z z'} e^{\frac{2\sigma_a z'}{\cos\theta_o}} \, dz'$$

$$\widetilde{\gamma}_2 = f(\sigma_a, \sigma_b) = \frac{(\sigma_a + \sigma_b) e^{i\phi(z_o)}}{\cos\theta_o (e^{(\sigma_a + \sigma_b) h_v / \cos\theta_o} - 1)} \int_0^{h_v} e^{ik_z z'} e^{\frac{(\sigma_a + \sigma_b) z'}{\cos\theta_o}} \, dz' \qquad \text{-13)}$$

$$\widetilde{\gamma}_3 = f(\sigma_b) = \frac{2\sigma_b \, e^{i\phi(z_o)}}{\cos\theta_o (e^{2\sigma_b h_v / \cos\theta_o} - 1)} \int_0^{h_v} e^{ik_z z'} e^{\frac{2\sigma_b z'}{\cos\theta_o}} \, dz'$$

Equation 13 shows that the maximum coherence is obtained for the medium eigenpolarisation with the highest extinction. This makes physical sense as the polarisation with highest extinction has the minimum penetration into the vegetation and hence the smallest amount of volume decorrelation. Similarly, the lowest coherence is then obtained for the orthogonal polarisation, which has the minumum extinction and hence better penetration into the vegetation and more volume decorrelation. The cross polar channel, which propagates into the volume on one eigenpolarisation and out on the other, has a coherence between these two extremes. Clearly for foliage penetration the lowest extinction is the most useful. If the vegetation cover is strongly oriented then direct use of 13 via the optimisation process in equation 12 can be used to align the radar co-ordinates with the eigenstates and hence select the polarisation that obtains minimum extinction by the vegetation.

However in many applications, especially at higher microwave frequencies, forest cover will be random and any orientation effects are likely to be weak [7]. For this reason, to deal with higher frequency problems we must consider a special case of equation 13 when the vegetation shows full azimuthal symmetry in the plane of polarisation [4]. In this case the coherency matrix [T] for the volume is diagonal with 2 degenerate eigenvalues of the form shown in equation 14 [3].

$$[T_v] = m_v \begin{bmatrix} 1 & 0 & 0 \\ 0 & \eta & 0 \\ 0 & 0 & \eta \end{bmatrix} \quad 0 \leq \eta \leq 1 \qquad \text{- 14)}$$

where η depends on the mean particle shape in the volume and on the presence of multiple scattering [4]. More importantly, the eigenvalues in equation 13 must become equal. This arises when $\sigma_\alpha = \sigma_\beta = \sigma$ i.e. when the extinction in the medium becomes independent of polarisation.

Figure 2 summarises this special case. Here we show a target covered by a vertical layer of vegetation of thickness h_v, inside of which the wave is extinguished by a scalar extinction coefficient σ as shown. It follows from equation 13 that the observed phase fluctuations or coherence for the volume only case is given by equation 15, where T_v is the diagonal polarimetric coherency matrix of the vegetation (equation 14). Here we see a ratio of volume integrals that is independent of polarisation i.e. the observed coherence will be the same for all polarisation channels w. The penetration depth is the same for all polarisations and the fixed phase centre lies somewhere between half the vegetation height and the top as we now show.

$$\hat{\gamma}_v = \frac{\underline{w}^{*T} \int\limits_0^{h_v} e^{\frac{2\sigma z'}{\cos\theta_o}} e^{ik_z z'} T_V dz' \, \underline{w}}{\underline{w}^{*T} \int\limits_0^{h_v} e^{\frac{2\sigma z'}{\cos\theta_o}} T_V dz' \, \underline{w}} = \frac{m_v \int\limits_0^{h_v} e^{\frac{2\sigma z'}{\cos\theta_o}} e^{ik_z z'} dz'}{m_v \int\limits_0^{h_v} e^{\frac{2\sigma z'}{\cos\theta_o}} dz'}$$

$$= \frac{2\sigma}{\cos\theta_o (e^{2\sigma h_v / \cos\theta_o} - 1)} \int\limits_0^{h_v} e^{ik_z z'} e^{\frac{2\sigma z'}{\cos\theta_o}} dz' \gamma_v$$

$$= f(h_v, \sigma) = \frac{p_1 (e^{p_2 h_v} - 1)}{p_2 (e^{p_1 h_v} - 1)} \qquad \begin{cases} p_1 = \dfrac{2\sigma}{\cos\theta_o} \\[2mm] p_2 = \dfrac{2\sigma}{\cos\theta_o} + ik_z \end{cases}$$

- 15)

In the limit that the extinction σ is zero, equation 15 reduces to the elementary sinc function as shown in 16. This shows that the vegetation layer causes a phase shift or vegetation bias given by half the vegetation height. As the extinction increases, this phase offset moves up in the canopy, until for very high extinction there is no penetration and the vegetation bias equals the vegetation height.

$$\hat{\gamma}_v \big|_{\sigma \to 0} = e^{ik_z \frac{h_v}{2}} \frac{\sin\left(\dfrac{k_z h_v}{2}\right)}{\dfrac{k_z h_v}{2}}$$

- 16)

Note that the phase variance or coherence is also a function of height. As the height increases so the coherence initially drops. Hence in order to obtain a good estimate of the phase we need to employ multi-look averaging. The detailed statistics of fluctuations in estimates of phase and coherence were first developed by Lee et al. [8] and further analysed by Touzi et al [11]. However, a simplified analysis provides convenient expressions for the Cramer-Rao bounds on the variance of the estimates as shown in equation 17 [9]

$$\text{var}_\phi > \frac{1 - |\gamma|^2}{2N |\gamma|^2} \qquad \text{var}_\gamma > \frac{\left(1 - |\gamma|^2\right)^2}{2N}$$

- 17)

Here N is the equivalent number of looks in the averaging process. We see that as N increases so the variance of the estimates decreases and that the phase variance increases with decreasing coherence.

We conclude from this analysis that if orientation effects are present in vegetation cover then polarimetric interferometry can exploit this to select a channel with the minimum extinction and hence achieve optimum foliage penetration. This maximum penetration channel corresponds to the minimum eigenvalue of the coherence optimiser. However, to counter this we have seen that when the vegetation becomes random then the extinction no longer varies with polarisation. In this case we seem to have no choice but to employ a longer wavelength that leads to a low extinction. However, by exploiting the polarimetric sensitivity of interferometric coherence to the presence of a target beneath the random vegetation, we can offset this requirement to achieve significant sub-clutter visibility as we now show.

B.2. Two-Layer Vegetation Model for Target Detection

In the previous section we considered the vegetation layer alone. Here we extend the analysis to consider a 2 –layer problem consisting of a random vegetation layer above a localised scattering centre, which acts as a model for a vehicle or other target beneath the canopy [7,10]. Figure 2 shows the geometry to be considered. We assume homogeneity in the y-direction and so consider only z or height variations. In this way the problem can be specified by a 1-dimensional vertical profile function d(z) as shown. The vegetation is modelled as a random volume with scalar extinction σ. The target is located at some unknown depth z_o and has an apparent magnitude m_g. Note that the azimuthal symmetry assumption applies only to the vegetation layer and that the target can have arbitrary form (including rotations due to sloped terrain/target orientation etc.). The observed coherence must now be modified from equation 15 to account for the presence of the target. This we can do as shown in equation 18, where the angles ϕ_1 and ϕ_2 are the phase centres of the target and bottom of vegetation layer respectively.

$$T_{11} = I_1^V + e^{-\frac{2\sigma h_v}{\cos\theta_o}} I_1^G \qquad\qquad \Omega_{12} = e^{i\phi_2} I_2^V + e^{i\phi_1} e^{-\frac{2\sigma h_v}{\cos\theta_o}} I_2^G$$

$$I_1^V = e^{-\frac{2\sigma h_v}{\cos\theta}} \int_0^h e^{\frac{2\sigma z'}{\cos\theta_o}} T_V dz' \qquad\qquad I_1^G = \int_0^h \delta(z') e^{\frac{2\sigma z'}{\cos\theta_o}} T_g dz' = T_g$$

$$I_2^V = e^{-\frac{2\sigma h_v}{\cos\theta}} \int_0^h e^{\frac{2\sigma z'}{\cos\theta_o}} e^{ik_z z'} T_V dz' \qquad I_2^G = T_g$$

$$\text{- 18)}$$

Collecting terms we can write the coherence as shown in equation 19, which also shows explicitly the polarisation dependence of the total observed coherence.

$$\tilde{\gamma} = \frac{\underline{w}^{*T}(e^{i\phi_2} I_2^V + e^{-\frac{2\sigma h_v}{\cos\theta_o}} T_g e^{i\phi_1})\underline{w}}{\underline{w}^{*T}(I_1^V + e^{-\frac{2\sigma h_v}{\cos\theta_o}} T_g)\underline{w}} = \frac{\underline{w}^{*T}(e^{i\phi_2} v^{-1} I_2^V + e^{i\phi_1} v^{-1} T_g)\underline{w}}{1 + \underline{w}^{*T} v^{-1} T_g \underline{w}}$$

$$v^{-1} = \frac{1}{\underline{w}^{*T} I_1^V \underline{w}}$$

$$\hat{\gamma}(\underline{w}) = e^{i\phi_1} \frac{\hat{\gamma}_v + \mu(\underline{w})}{1 + \mu(\underline{w})} = e^{i\phi_1}\left(\hat{\gamma}_v + \frac{\mu(\underline{w})}{1 + \mu(\underline{w})}(1 - \hat{\gamma}_v)\right)$$

$$= e^{i\phi_1}\left(\hat{\gamma}_v + L(\underline{w})(1 - \hat{\gamma}_v)\right) \qquad 0 \le L(\underline{w}) \le 1$$

$$\text{- 19)}$$

The parameter μ is the target-to-volume scattering ratio and is defined in equation 20

$$\mu(\underline{w}) = \frac{2\sigma}{\cos\theta_o(e^{\frac{2\sigma h_v}{\cos\theta_0}} - 1)} \frac{\underline{w}^{*T} T_g \underline{w}}{\underline{w}^{*T} T_V \underline{w}} \ge 0$$

$$\text{- 20)}$$

Since both T matrices in equation 20 are Hermitian, it follows that μ is a positive semi-definite function. We see that the presence of a target beneath the canopy influences the observed coherence. If the target scattering changes with polarisation then this will be reflected in changes in the observed coherence. Hence by using polarimetric interferometry we can detect the presence of targets by looking at the variation of coherence with polarisation. For vegetation only this will yield zero or small changes, however bright the

canopy return. However, when a target is present the changes will be larger hence enabling sub-clutter visibility of targets.

We note from equation 19 that we can write the coherence in terms of a real function L that varies from 0 to 1. This defines a line in the complex plane inside the unit circle [10]. Figure 3 shows a geometrical representation of this line. We see that by measuring the coherence and relating it to the end points we can estimate μ the ground-to-volume scattering ratio for that polarisation. The red (left) point is the μ=0 or volume coherence alone. This we can approximate by measuring the coherence in a channel with small-expected target signal, the cross-polarised HV channel for example. The yellow (right) point is the bare earth topography and is not directly visible in the data because of the vegetation cover. However by extrapolating the line beyond its visible length we can estimate the bare earth topography from the unit circle intersection [10].

$$\mu(\underline{w}) = \frac{\hat{\gamma}_v e^{i\phi_1} - \hat{\gamma}(\underline{w})}{\hat{\gamma}(\underline{w}) - e^{i\phi_1}}$$

$\tilde{\gamma}_v e^{i\phi_1}$

$\tilde{\gamma}(\underline{w})$

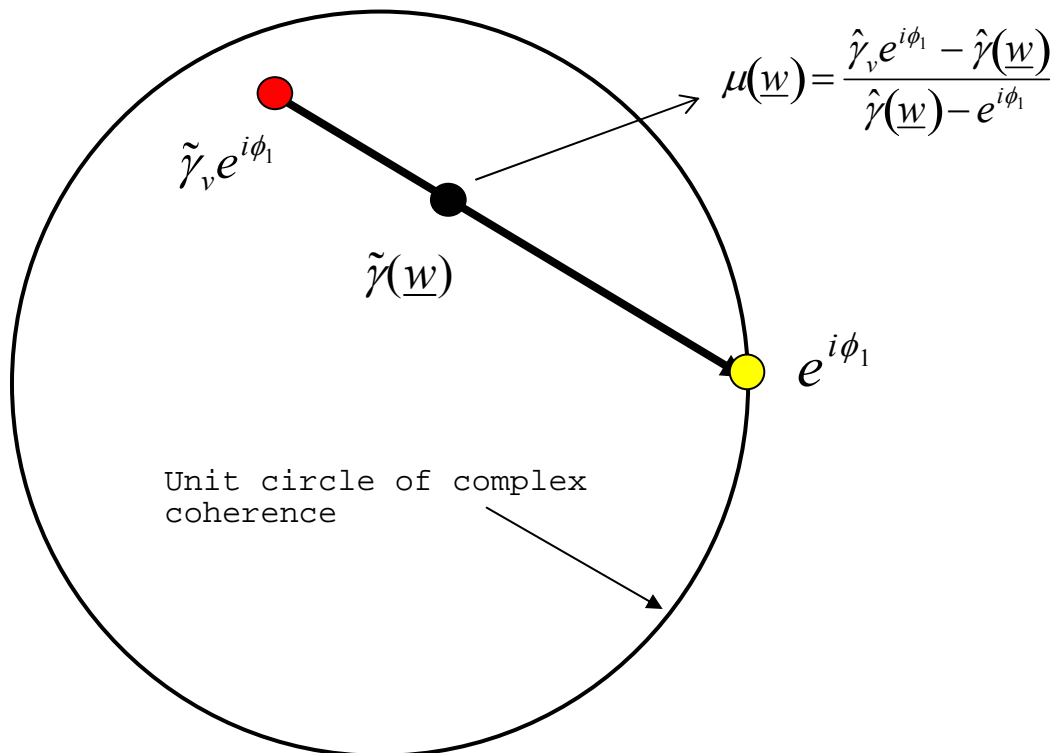$e^{i\phi_1}$

Unit circle of complex coherence

Figure 3: The line coherence model for target+random volume scattering

Note that we obtain an ambiguity with this method as there will be two such intersection points, only one of which will correspond to the true ground topography. This can be resolved using rank ordering of coherence or a reference digital terrain model (DTM) for the scene [10].

Having identified a mechanism by which targets can be detected, we now investigate the sensitivity of the method to the presence of target scattering. To do this we calculate the derivative of coherence with respect to the target-to-volume ratio as shown in equation 21

$$\frac{\partial \hat{\gamma}}{\partial \mu} = \frac{(1 - \hat{\gamma}_v)}{(1 + \mu)^2} = f(\mu)g(\hat{\gamma}_v)$$

- 21)

We are particularly interested in the case where μ is less than 1, this being a situation where the volume scattering is larger than that from the target. Equation 21 is the product of 2 terms. Concentrating first on the μ dependence, we can express this sensitivity by calculating the function L in equation 19, being the fractional change in the length of the line due to a presence of a target. We see that even with −10dB of

scattering ratio, the shift in coherence is about 10% of the line length. The line length itself is $\left| 1 - \hat{\gamma}_v \right|$. Hence in order to be able to detect a small change we need to choose the baseline so that the length is maximised. This would seem to require that $\gamma_v = -1$ i.e. the baseline is chosen so that the vegetation phase centre lies at the π height. However this must also occur with a coherence magnitude of unity. Examination of equation 15 shows that this requires infinite extinction in the medium. Clearly this is not a practical solution and hence in practice the optimum baseline will be a function of both height and wave extinction. As an example, figure 4 shows how the line length varies with increasing k_z for typical values of 10m high trees and 0.3 dB/m one way extinction. Note that the line length (in red) increases to a maximum before decreasing again and then shows oscillatory behaviour.
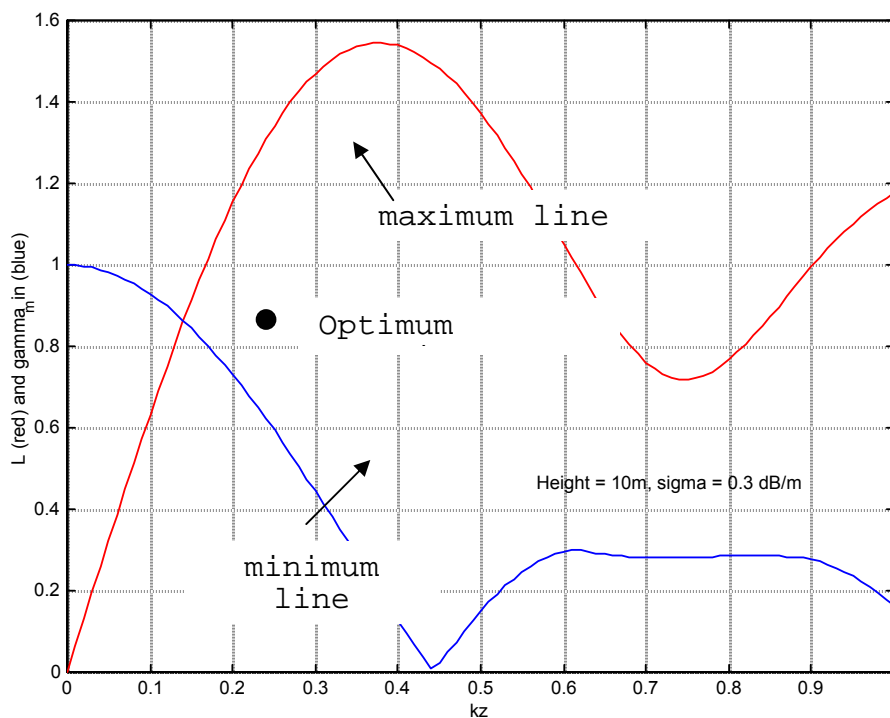

Figure 4: Line length variation with increasing baseline and minimum coherence along the line. The intersection point represents a compromise between sensitivity and resolution.

There is one additional feature that bears on this question of optimum line length, namely the need to estimate complex coherence from the data itself. There are two issues, the first is the need for a large effective number of looks when the coherence is low. This follows from the Cramer Rao bounds in equation 17. If the coherence line goes through the origin for example then the phase becomes indeterminate. The need for a high effective number of looks (ENL) is serious because it impacts on the resolution requirements of the sensor and also leads to a reduced μ value. This arises since, for point targets, the volume clutter increases with the ENL while the target RCS does not. Hence we need to minimise the ENL and so maximise the minimum line coherence value. The second issue relates to the fact that coherence techniques based on standard box-car averaging provide biased estimates at low coherence [11]. While this bias reduces with increasing coherence and number of looks it tends to overestimate low values of coherence. This is serious as it will give a radial bias to low coherence values and hence distort the line parameter estimates. To solve this we must either use unbiased coherence techniques or set a lower limit (set by the ENL) on the minimum line coherence.

In either case we seek to maximise the minimum line distance from the origin. By itself this leads us to choose a zero baseline, as then all coherences are 1. However, when combined with the need to maximise L it leads us to a compromise optimum baseline. This minimum line coherence is shown in blue in figure 4.

We see that the two curves intersect at one point. This is the optimum for that configuration. It combines good sensitivity to target scattering and also minimises the ENL required for good estimates. In this case we obtain a k_z value around 0.15. In general it will be a function of height and extinction. Global mean tree heights lie around 20m and this leads to a rough interferometer design figure of $k_z = 0.1$. The most important factor in determining the best baseline is the tree height. It should be pointed out that this parameter can itself be estimated from the data using polarimetric interferometry techniques [7,10] and hence the optimum baseline can in principle be adapted 'in the field' to match local conditions.

Our proposed POLINSAR target detection algorithm is then based on estimation of a scalar radar parameter μ, obtained from complex interferometric coherence estimates in different polarisation channels w. The parameter μ is dimensionless, being the ratio of all scattered power contributions with an apparent phase centre located on the surface, to the total volume scattering. The former includes direct surface returns, the desired target backscatter as well as dihedral effects caused by specular surface scattering and secondary interactions with the vegetation (ground-trunk returns). The volume returns include all scattering (single and multiple) with phase centres displaced from the surface. It follows from this that the presence of a target corresponds to a local maximum in μ. Further, from the conventional SAR intensity channel we obtain an estimate of the sum of these two contributions s(w) as shown in equation 22.

$$s(\underline{w}) = \frac{\cos\theta_o(1 - e^{-\frac{2\sigma h_v}{\cos\theta_0}})}{2\sigma} \underline{w}^{*T} T_V \underline{w} + e^{-\frac{2\sigma h_v}{\cos\theta_0}} \underline{w}^{*T} T_g \underline{w}$$

- 22)

Hence we can solve equations 20 and 22 to obtain an estimate of the surface scattering components as shown in equation 23

$$\underline{w}^{*T} T_g \underline{w} = e^{\frac{2\sigma h_v}{\cos\theta_0}} \frac{\mu(\underline{w})}{1 + \mu(\underline{w})} s(\underline{w})$$

$$= e^{\frac{2\sigma h_v}{\cos\theta_0}} L(\underline{w}) s(\underline{w}) = e^{\frac{2\sigma h_v}{\cos\theta_0}} F(\underline{w}) \quad 0 \le L(\underline{w}) \le 1$$

- 23)

The function L(w) acts as a filter on the intensity channel to produce an image domain with better signal to clutter ratio. Note that because we always see the ground components through the canopy, they are influenced by the local extinction and height of the vegetation as shown in 23. However, all ratios between polarisation channels (such as HH/VV etc.) are independent of height and extinction (under the assumption of a random volume). This is important for target classification studies. Using the above results we can now devise a general algorithm for target detection using polarimetric interferometry.

B.3. POLINSAR Target Detection Algorithm

We assume access to two single look complex fully polarimetric SAR images that have been co-registered and phase and amplitude calibrated. We also assume that there are no temporal decorrelation or signal to noise ratio problems in the data. We then propose a generic processing chain as follows:

Stage 1 : Coherence Estimation

The first stage is to generate complex coherence estimates for a number of polarisation states w. In all cases, equation 5 is used with the appropriate w vectors. For simplicity we adopt a boxcar averaging process for coherence estimation, employing an M x M window centred on the pixel of interest. However we must realise that this will lead to coherence bias for low coherence values, as discussed in [11]. It will also lead to edge effects on the boundaries between different scatterer types, when the true coherence will be

underestimated because of mixed scattering mechanisms. Here we ignore such effects but note that forest edges are of significant tactical importance in hidden target applications. Initial development of coherence estimators that are more suitable for such problems are presented in [12].

Stage 2 : Least Squares Line Fit

The next stage is to find the best-fit straight line to the polarimetric coherence values inside the unit circle (using a reference DTM if available to fix the unit circle intersection point). From these line parameters we then project each of the measured complex coherence values γ_i onto the least squares line. This projection then ensures real μ estimates as required in equation 20.

Stage 3 : Select the reference volume coherence channel

For single baseline systems we cannot estimate the volume coherence point uniquely [10]. There are a set of candidate volume coherence values defined geometrically as all points on the line which lead to an observed positive semi-definite function $\mu(\omega)$. Nonetheless, in practice we can select a polarisation channel we expect to be close to the true volume point. Often this will just be the cross polar HV channel, where we expect a small target-to-clutter ratio in most cases. In this study we employ the HV channel throughout. A more general strategy is to employ the polarisation with maximum vegetation bias [10].

Stage 4 : Estimate Ground Scattering Components and Filtered Intensity

Having estimated the extreme points on the coherence line, we can now estimate the μ value in any desired polarisation channel. Figure 5 shows how we can estimate these two values for the HH+VV and HH-VV channels matched respectively to trihedral and dihedral scatterers. Here we show two cases, background clutter (lower) and the presence of a target (upper). From μ we can then obtain L(w) using equation 19. We then estimate the mean backscatter intensity in the w channel using a the same boxcar average as for the coherence and finally multiply this intensity by the function L to obtain F(w).
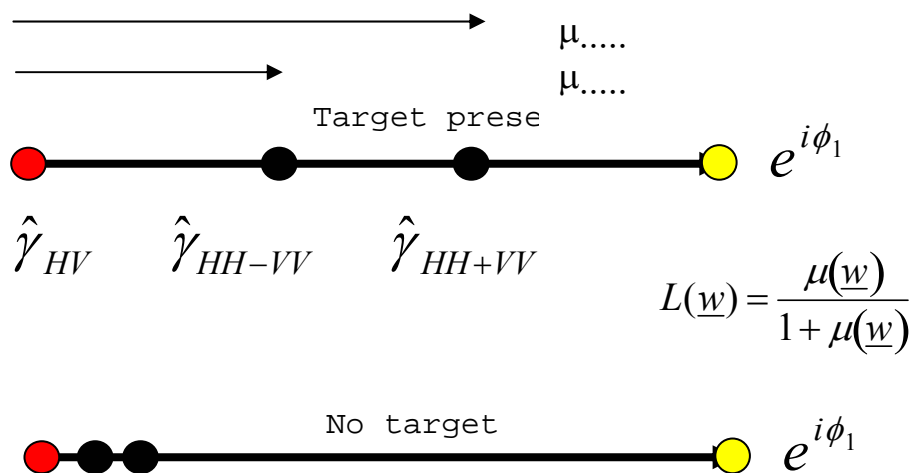

Figure 5: Polarimetric target-to-volume scattering ratio estimation.

To quantify the potential of this method to suppress forest clutter and provide enhanced detection, we now turn to consider its application to simulated POLINSAR data.

B.4. POLINSAR Target Simulations

To enable an assessment of algorithm performance, a Maxwell equation based wave propagation and scattering model is used to generate test image data for trihedral and dihedral corner reflectors embedded in foliage clutter. Several approaches to the modelling of coherent forest microwave scattering have been developed in the literature [13-17]. Our simulation employs a 3-D voxel-based, vector wave propagation and scattering model coupled to a detailed description of tree architecture and forest structure [15-17]. The SAR simulation is fully polarimetric, coherent and deterministic, and so may be used to model volume decorrelation effects, as required in polarimetric SAR interferometry.

Simulation of the SAR images is a multistage process that begins with the construction of a detailed computer model of the scene to be imaged. This model incorporates a digital terrain map (DTM) of the underlying surface (generated artificially or supplied from observation), and soil description parameters including local roughness, correlation length, soil type [18] and moisture content. A map of tree heights and locations is calculated that corresponds closely to observed distributions [16], the stand density employed here being moderate at 0.055 stems/m^2, with a mean height of 18m and height standard deviation of 0.6m. The forest canopy is populated with Scots Pine tree models in the form of collections of layered, dielectric cylinders calculated according to biologically determined growth rules [15]. The tree models are architecturally correct (see Figure 6.) and include details of the size and distribution of pine needles along living branches. The water contents of deadwood, sapwood, heartwood and pine needles [16] complete the physical description of the forest canopy. Finally, targets, modelled as collections of perfectly conducting, interacting surfaces, are positioned throughout the scene. Modelled in this fashion, the forest canopy represents a distribution of discrete, dielectric objects. As such L-Band scattering by the canopy may be calculated using the mean-field approach pioneered by R H Lang [19, 20], and subsequently extended to layer geometry and employed in backscatter modelling of grass canopies [21] and of forest canopies at C-band [22]. The mean–field approach is a coherent wave model that approximates the locally incident field at any discrete scattering object by the mean wave propagating in the layer, and calculates scattering using a Green's function for the mean wave.

For a homogeneous medium the Green's function for the mean wave is everywhere the same. However the forest canopy is inhomogeneous on a scale commensurate with the resolution of the SAR system and it is desirable to incorporate the effects of canopy inhomogeneity into the simulation. In this way targets deployed so as to be visible to the SAR sensor through gaps in the canopy will not appear attenuated by some global mean attenuation constant. To achieve this we employ the form of the layered Green's function of the mean wave [20,21], but estimate the wavenumber of the mean wave locally for the aperture used to focus each scattering interaction. In practice this entails dividing the canopy volume into sub-volumes (voxels) on a scale determined by the sensor resolution, and such that each voxel contains a large number of scattering objects. The detailed forest model is used to determine the occupancy of each voxel, and then effective permittivity of the voxel is calculated using the Foldy-Lax approximation [21, 22] with vegetation permittivities determined using the model described in [24] at frequencies used by the SAR instrument. Tree branches are divided into many elements in order to better estimate voxel volume fractions. To calculate backscatter from any element of the scene the effective wavenumber is determined using the mean properties of voxels intercepted by the line of sight between the current sensor position and the scene element. The dependence of the effective wavenumber, and hence of the attenuation of scattering amplitudes, both upon frequency and polarisation, arises naturally in the model from the physical and biophysical descriptions.

SAR is a coherent imaging process, and thus the mean field model is an appropriate model to adopt in the simulation. Scattering of the coherent, mean wave is focused by the SAR instrument using the phase history of the scattered signal [25]. Coherent phase histories are modelled in the simulation, but the contribution to the image from scattering of the incoherent wave is not modelled directly. This may be incorporated in the form of a noise signature. Calculation of simulated SAR images proceeds by forming the coherent superposition of focused scattering events, each arising from a scene element much smaller than the SAR system resolution. The simulated SAR image may be described as

$$\underline{\underline{P}}(x_0, R_0) = \sum_j \underline{\underline{F}}_j \, \hat{Q}(x_0, R_0, \underline{s}_j)$$

- 24)

where $\underline{\underline{P}}(x_0, R_0)$ is the polarimetric pixel value at cross range x_0 and range R_0, $\underline{\underline{F}}_j$ is the polarimetric scattering amplitude associated with the scene element, and $\hat{Q}(x_0, R_0, \underline{s}_j)$ is the complex system point spread function depending upon the effective scattering centre $\underline{s}_j$. Scattering amplitudes $\underline{\underline{F}}_j$ may be calculated as averages both in azimuth (along the synthetic aperture) and frequency (across the SAR bandwidth). The system point spread function $\hat{Q}$ is determined from the specified SAR imaging geometry, bandwidth and processing options. The platform motion is ideal, and the platform is modelled as having a straight, uniform trajectory. Each scene element has an effective scattering centre, which determines the point of focus of backscatter in the two dimensional SAR image. For first order or direct backscatter the effective scattering centre is simply the centre of the scene element. For higher order returns, involving multiple reflections, the effective scattering centre is determined rapidly at run-time using knowledge of the scattering path and the antenna motion. The centre of focus in the SAR image is simply the projection of the effective scattering centre onto the SAR imaging plane, which may be calculated using near-field or far-field models. Simulated single-look, complex SAR images are output in ground range and azimuth.

Direct-ground contributions are calculated from ground facet elements using a hybrid deterministic/stochastic approach. Ground facet RCS values depend on local incidence through a physical scattering model (the Bragg or small perturbation model), to which speckle is added. Local speckle statistics are assumed Gaussian and scattering amplitude values are drawn from distributions using the mean RCS for the facet as determined from local incidence. A spatially correlated speckle phase model may be used which depends upon surface roughness, surface correlation length, wavelength and incidence angle. The correlated speckle phase model reduces to spatially uncorrelated speckle phase for short wavelength and surface correlation length, as well as for large surface roughness. To calculate direct forest clutter, each branch element is addressed in turn with scattering amplitudes calculated using the mean field and truncated, infinite cylinder approximations [26]. No calculation of multi-path between tree elements is performed since this has in theory already been taken into account in the mean-field model. We note however that for correct calculation of cross-polar returns at higher frequencies than L-band the explicit incorporation of such multiple interactions may be necessary [27]. Needle scattering is estimated in a statistical manner, by simulating short random walks using a generalised Rayleigh-Gans scattering model for needles [28], and scaling these short walks depending upon the number of needles associated with each branch element.

In general the ground has arbitrary roughness and many different scales of variation in height. Calculations are limited to the case that the ground may be assumed locally flat, but roughened and tilted. Local orientation of the mean surface for ground-element interactions is calculated from the mean slope close to the scattering element. Ground-element interactions have effective scattering centres located as the normal projection of the true scattering centre in the locally flat, mean surface. Similarly, ground-element-ground interactions have effective centres located at the reflection of the element centre in the locally flat, mean surface.

Targets are modelled as collections of perfectly conducting surfaces. Each of the target surfaces is divided into triangular facets of dimension much less than the system resolution. Multipath scattering amplitudes are calculated for each facet in the final surface of a multipath scattering chain using the geometrical optics, and physical optics approximations [29]. This model yields accurate RCS estimates, and preserves the expected polarimetric responses of known targets types. The effective scattering centre for each such surface facet is calculated by tracing the history of the specular path of a multipath event during formation of the synthetic aperture. This approximation is consistent with the geometrical optics model used for all but the last scattering interaction in any surface scattering chain. Interactions involving up to three surfaces are considered in the calculations, which include surface shadowing effects [17]. The method of specular path tracing lends itself readily to the modelling of multipath between ground and target when the ground is essentially locally flat (over the region traversed by the specular point) and only slightly rough: the ground acts as a primary reflecting surface in the multipath chain. Ground and target surfaces are distinguished only by their reflection properties: the ground is modelled as a rough dielectric surface, with Fresnel reflection coefficients scaled according to the surface roughness using the Rayleigh roughness parameter [30].

Effective scattering centres for direct-element, ground-element and ground-element-ground interactions lie respectively above, close-to and below the ground surface. Thus a simulated SAR image of a forest contains a direct-canopy image, displaying layover of tree direct reflectivity towards the radar, a ground-canopy image displaying projection of the ground-tree reflectivity onto the local mean ground surface, and a ground-canopy-ground image displaying layover away from the radar. At L-band the ground-canopy and direct-canopy terms appear to influence most strongly the total clutter level and the ground-canopy-ground terms are negligible. Predictions for forest clutter at L-band at 45 degrees elevation of –4dB (HH) –11dB (HV) and –8dB (VV) are consistent with those reported in the open literature for similar forests [31].

B.5. Simulation Results

Figure 6 shows model detail of a single tree (on the left) and an optical view of the entire pine forest scene to be simulated (on the right). Embedded in this scene is an array of 27 square corner reflectors. They are a mixture of trihedrals and dihedrals at two orientation angles, namely 0° and 22.5^o, the latter guaranteeing a strong cross-polar response. The details of the target array are shown in figure 7. Three sizes of reflector are used, 90, 60 and 30cm. In this way we model a range of different target responses in both polarization and radar cross section. The spacing between targets is 14m.
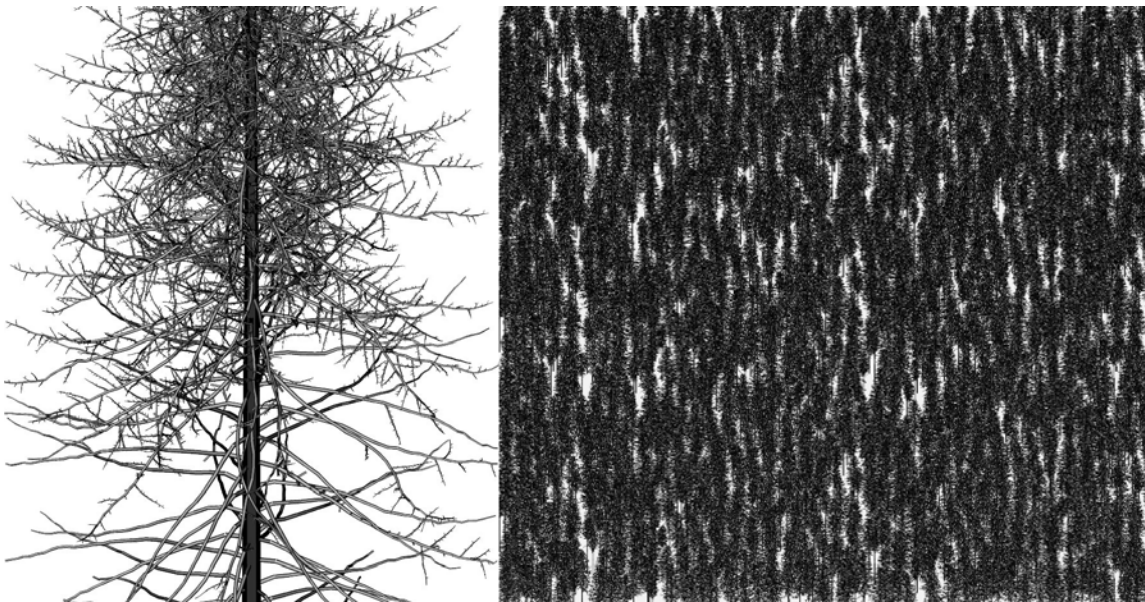

Figure 6: Detail of an individual tree drawn without needles (left) and view from aperture centre of the simulated forest stand (150m x 150m) with hidden in-situ corner reflector array (right).
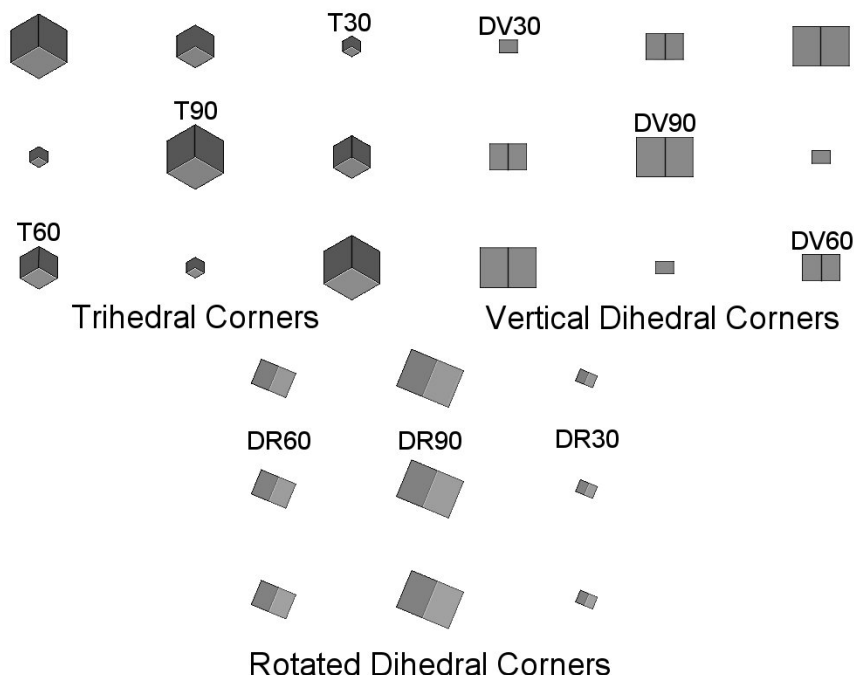
Figure 7: Details of the corner reflector array: TXX is a trihedral of dimension XX cm, DVXX is a vertical dihedral, DRXX is a dihedral rotated at 22.5 degrees. The targets are shown with exaggerated dimensions for clarity.

We model the radar response at L-band or 23cm wavelength. Analysis of the model with and without vegetation in place then enables estimation of the mean wave extinction σ. For V polarization this corresponds to a 1-way attenuation rate of 0.28 dB/m while for H polarization the extinction is lower, with a mean value around 0.14 dB/m. Hence the model predicts some departure from the azimuthal symmetry assumption required for the FOPEN algorithm. We found however that the algorithm is fairly robust to such levels of differential extinction, although they do seem to act in limiting detection of the smaller targets (see figure 10). Future studies and field experiments will investigate the effects of differential extinction in more detail.

For validation reasons, we start with a system configuration closely matched to the DLR E-SAR airborne L-band system [7], which typically operates at an altitude of 3km with a 45-degree angle of incidence in the centre of the swath. The transmitted bandwidth is 100 MHz and the synthetic aperture yields an azimuth resolution around 0.75m. We simulate these conditions to obtain an effective sensor resolution of 1.38m in ground range and 0.69m in azimuth. The data is then over-sampled to obtain a square pixel size of 0.5m. Figure 8 shows simulated L-band SAR imagery for this scene. Four images are shown, corresponding to the four transmitter/receiver polarization combinations. We note that it is difficult to see the corner reflectors in the background foliage clutter, although for example in the cross-polar channel some of the rotated dihedrals can be seen.

Figure 9 shows the single look interferometric phase for this scene. In the upper portion we show the raw phase and in the lower the residual phase following flat earth removal of the spatial frequency variation in range due to changes of the angular separation of the antennas for a flat earth geometry. We see that the local topography is relatively flat with the presence of the trees causing volume decorrelation or increased

phase variance. Again in this single channel interferogram (the VV Channel) there is no clear indication of the presence of targets. It is only when we combine many such interferograms at different polarizations that we can detect the targets more clearly as modulations in the mean phase and variance. We now apply the processing algorithm of section 4 to interferograms in 2 channels, namely HH+VV and HV.
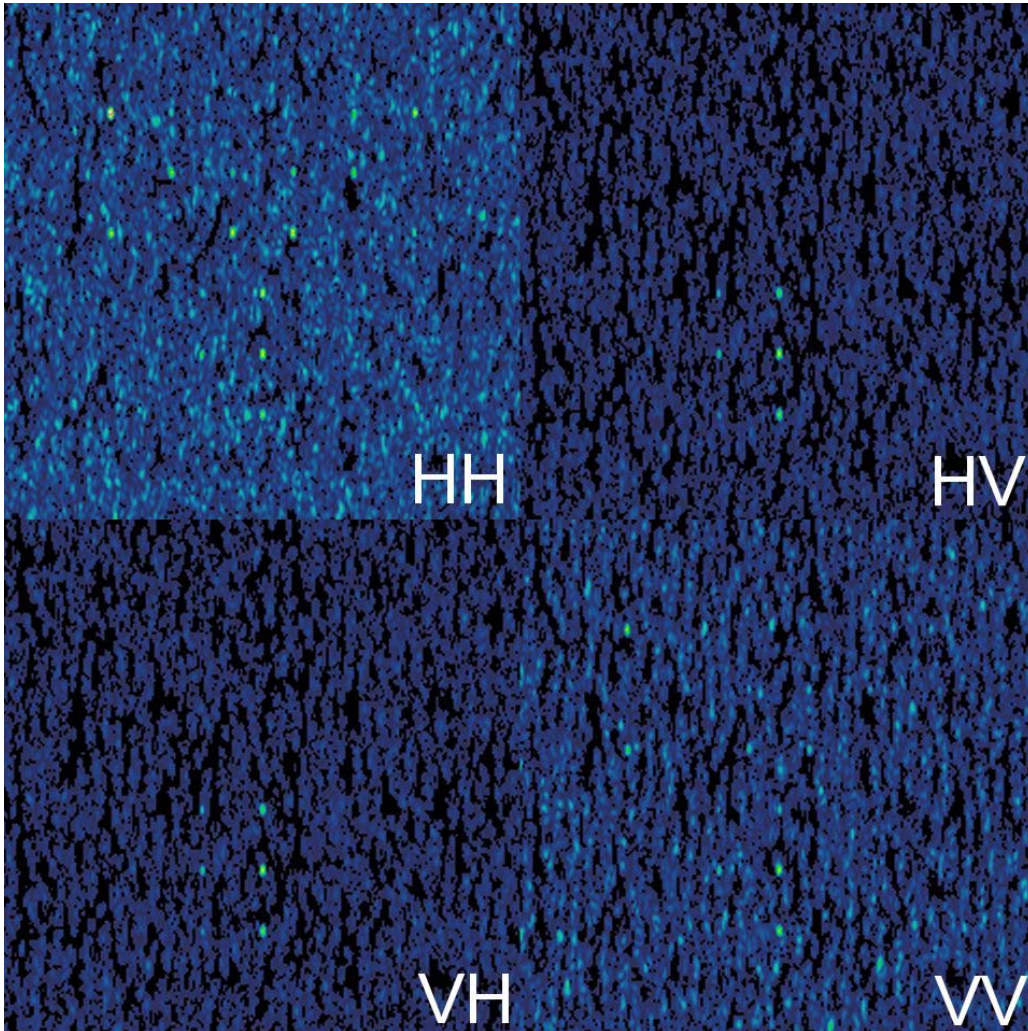

Figure 8: Simulated L-Band, polarimetric SAR Images of the corner reflector array deployed in the model forest.

To illustrate the level of processing gain achievable with multi-channel interferometry, we show in figure 10 a comparison of the unfiltered image intensity (using a 5 x 5 window) and the POLINSAR filtered intensity F(w). In both cases we display a dynamic range of 25dB of the peak signal in the scene. In this way we can quickly visualize any signal processing improvements. We have selected the HH+VV polarization channel corresponding to w = (1,0,0), which is matched to the presence of trihedral corner reflectors and so show only the portion of the image around the cluster of TXX targets in figure 7. By changing w we can select different target types in the scene but here we concentrate on the results for the trihedral reflectors only.

We can see that the large trihedrals (T90) are seen both in the raw and filtered intensity data but the T60 and T30 reflectors cannot be easily discriminated from the background clutter in the standard intensity channel. The filtered image however shows a strong reduction of the background clutter, allowing both the T90 and T60 reflectors to be much more clearly seen. We note that the T30 reflectors still cannot be detected. The reason for this can be traced to the   values for the three target types. We can obtain estimates of μ directly from the separate simulation of target and volume components in the SAR simulator. This analysis shows that T90 has μ = 5 dB, T60 has μ = -2dB and T30 μ = -10 dB. Analysis of residual orientation and structural

effects in the forest canopy also indicate a maximum filter suppression of –10dB. This explains the poor detection of T30 in this environment.

However, despite this, we note that the T60 elements are now much more clearly discriminated from their background. The impact of this on detection statistics is demonstrated in figure 11. Here we show 3-D images of the raw and filtered SAR channels. In the raw channel we see that the 60cm reflectors are obscured by background clutter, leading to a large number of false alarms in the detection process. In the filtered channel on the other hand we can see that the algorithm has suppressed the clutter while maintaining the signal from the target. In the case of the 60cm reflectors, setting a threshold of -3dB their peak value now obtains zero false alarms in the scene. We conclude that the POLINSAR processing gains are significant and warrant further studies of more complex vehicle targets embedded in forest clutter. We also plan further analysis of coherent random vector wave propagation and scattering effects in different forest environments to obtain a more robust assessment of algorithm performance.
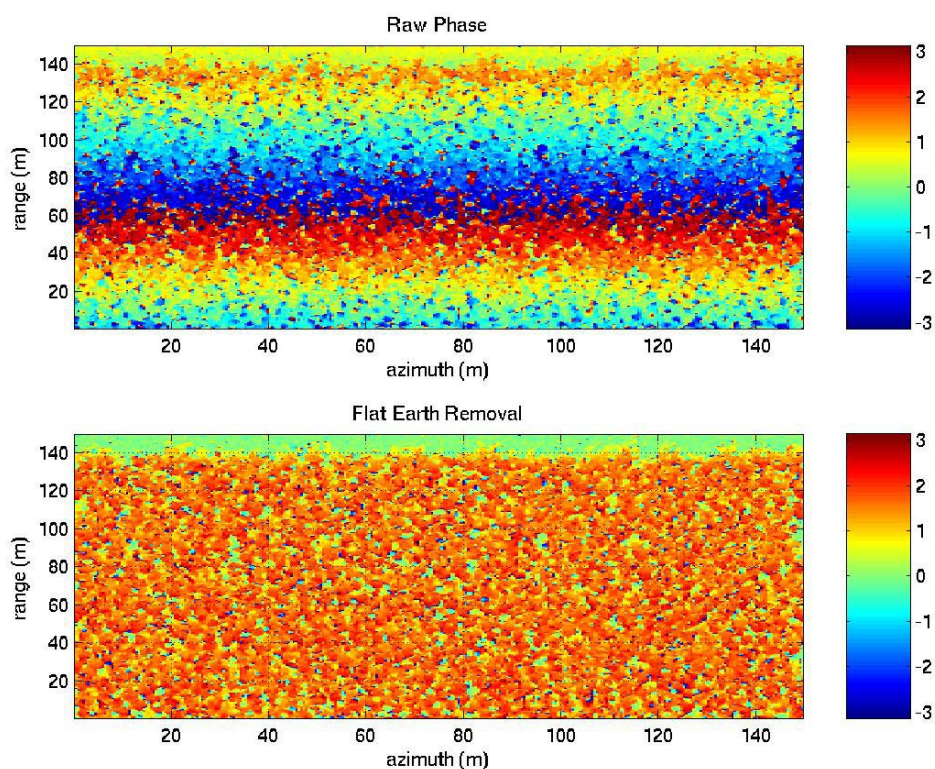

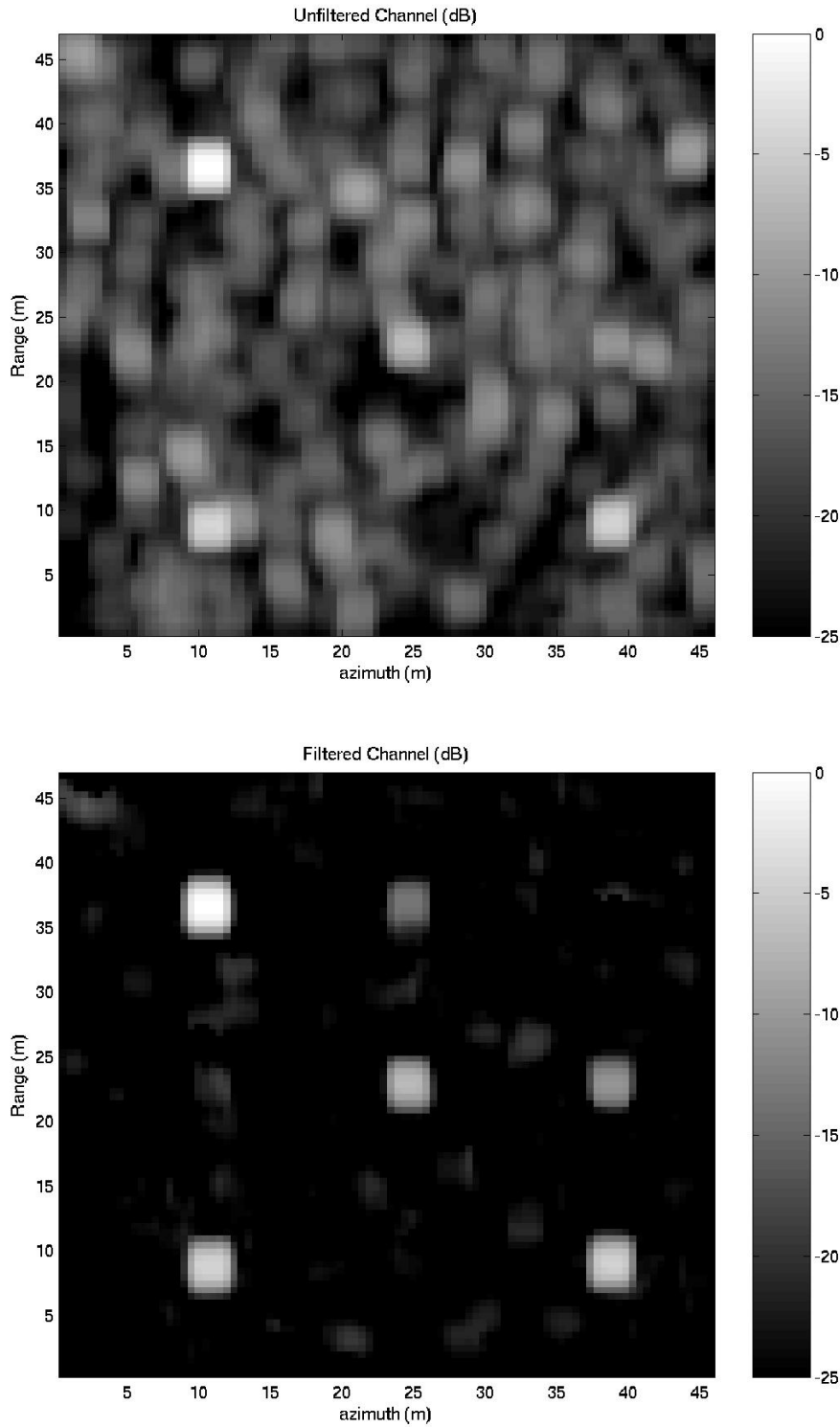Figure 9: Interferometric phase (upper) and residual phase following flat earth removal (lower) for forested scene.

Figure 10: Multi-look intensity (upper) and filtered intensity (lower) images of trihedral corner targets in foliage (5 x 5 window, HH+VV channel).
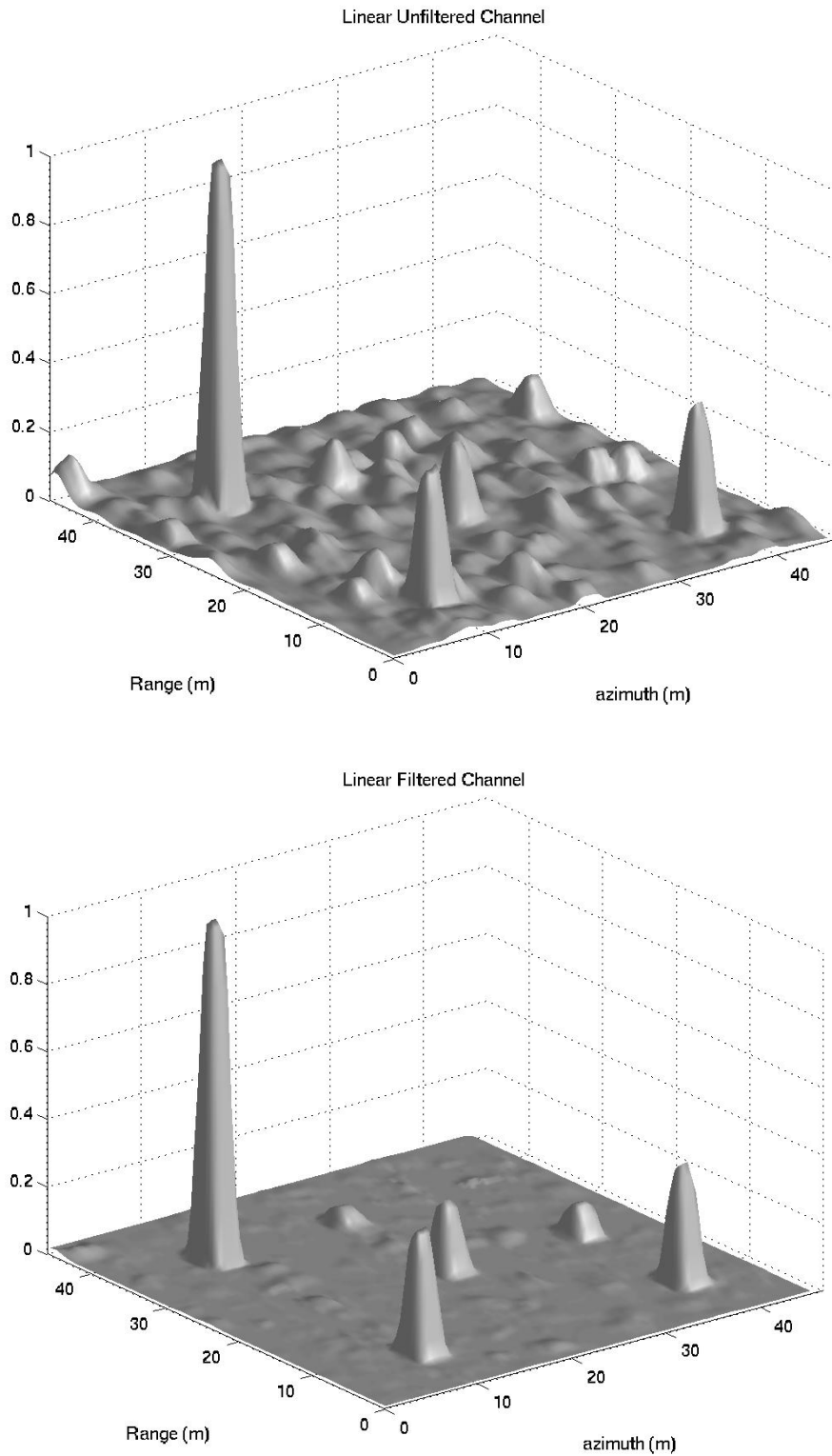
Linear Unfiltered Channel

Linear Filtered Channel

Figure 11: Normalised backscatter of trihedral sub-array for unfiltered HH+VV channel (upper) and POLINSAR filter output (lower)

B.6. Conclusions

In this section we have introduced the idea of combining multiple interferograms at different polarizations to enhance the detection of targets hidden by foliage. In the case where there are strong orientation effects in the volume scattering we have shown that the coherence optimizer can be used to select the polarization with minimum extinction and hence optimum penetration of the foliage. In the extreme case of random volume scattering, we have shown that we can design a filter based on the invariance of volume decorrelation to polarization state. The presence of a target beneath the volume then breaks this symmetry and leads to a linear variation of coherence inside the unit circle of the complex plane. By normalizing this variation to the distance between the ground topography unit circle and invariant volume decorrelation points, we can generate a filter with range 0 to 1. This filter then multiplies the intensity channel so that in regions where there is volume scattering only the intensity is reduced to zero while the target response is maintained. In this way the target to clutter ratio can be improved and targets detected using a threshold based on conventional constant false alarm rate (CFAR) techniques, applied now to the filtered intensity channel

We have illustrated the application of this method to data generated by a full vector wave based SAR simulator which takes as its input detailed three dimensional forest structural and target information, as well as details of the SAR point spread function and generates as output the complex SAR data which accounts for the phase of each scattering element in the scene. In this way the simulator can be used to model volume decorrelation as a function of polarization. We have made simulations of high resolution SAR imagery at 23cm wavelength (L-band) of a pine forest scene containing an array of corner reflectors of different sizes and orientations. In this paper we have concentrated on detection of a cluster of 9 trihedral reflectors and have shown significant improvements in detection performance. This suggests the possibility of enhanced target detection in foliage at the relatively high L-band frequency, which has many advantages in the future deployment of space and air borne systems. Future studies will address the detection of more complex target types such as vehicles and issues relating to improved sensor resolution.

B.7. Acknowledgements

B.8. References

[1] Bamler R, P. Hartl, 1998, "Synthetic Aperture Radar Interferometry", Inverse Problems, 14,R1-R54

[2] Gatelli F A Monti Guarnieri, F Parizzi, P Pasquali, C Prati, F Rocca, "The Wavenumber Shift in SAR Interferometry", IEEE Transactions on Geoscience and Remote Sensing. GRS-32, pp 855-865, July 1994

[3] Cloude S.R., K P Papathanassiou, "Polarimetric SAR Interferometry", IEEE Transactions on Geoscience and Remote Sensing, Vol 36. No. 5, pp 1551-1565, September 1998

[4] Cloude S.R., E. Pottier, "A Review of Target Decomposition Theorems in Radar Polarimetry", IEEE Transactions on Geoscience and Remote Sensing, Vol. 34 No. 2, pp 498-518, March 1996

[5] Treuhaft R.N. , S.R. Cloude,"The Structure of Oriented Vegetation from Polarimetric Interferometry", IEEE Transactions Geoscience and Remote Sensing, Vol 37/2, No. 5, p 2620-2624, September 1999

[6] Cloude S. R., K.P. Papathanassiou, W.M. Boerner, "The Remote Sensing of Oriented Volume Scattering Using Polarimetric Radar Interferometry", Proceedings of International Symposium on Antennas and Propagation, ISAP 2000, Fukuoka, Japan, pp 549-552, August 2000

[7] Papathanassiou K.P., S.R. Cloude, "Single Baseline Polarimetric SAR Interferometry", IEEE Transactions Geoscience and Remote Sensing, Vol 39/11, pp 2352-2363, November 2001

[8] Lee J S, K W Hoppel, S A Mango, A Miller, "Intensity and Phase Statistics of Multi-Look Polarimetric and Interferometric SAR Imagery", IEEE Trans GE-32, pp. 1017-1028, 1994

[9] Seymour S., Cumming I.G., "Maximum Likelihood Estimation for SAR Interferometry", Proceedings of IEEE International Geoscience and Remote Sensing Symposium (IGARSS94), Pasadena, USA, 1994

[10] Cloude S.R. , K.P. Papathanassiou, " A 3-Stage Inversion Process for Polarimetric SAR Interferometry", IEE Proceedings, Radar, Sonar and Navigation, Volume 150, Issue 03, pp 125-134, June 2003

[11] Touzi R, Lopes A., Bruniquel J, Vachon P.W., "Coherence Estimation for SAR Imagery", IEEE Transactions Geoscience and Remote Sensing, VOL. GRS-37, pp 135-149, January 1999

[12] Lee J.S., S.R. Cloude, K.P. Papathanassiou, M.R. Grunes, I. H. Woodhouse, "Speckle Filtering and Coherence Estimation of POLInSAR Data for Forest Applications", IEEE Transactions on Geoscience and Remote Sensing, Vol. 41, No. 10, pp 2254-2263, October 2003

[13] Lin Y.C. , K. Sarabandi, "A Monte-Carlo coherent scattering model for forest canopies using fractal generated trees", IEEE Transactions Geoscience and Remote Sensing, VOL. GRS-37, pp 440-451, January 1999

[14] Sarabandi K., J.C. Lin "Simulation of Interferometric SAR response for characterising the scattering phase centre statistics of forest canopies", IEEE Transactions Geoscience and Remote Sensing, VOL. GRS-38, pp 115-125, January 2000

[15] Kellomäki S., Veli-Pekka Ikonen, Heli Peltola and Taneli Kolström, "Modelling the Structural Growth of Scots Pine with Implications for Wood Quality", Ecological Modelling, 122, pp117-134, 1999.

[16] Williams M.L., T Manninen, Seppo Kellomäki, Veli-Pekka Ikonen, Risto Sievänen, Mika Lehtonen, Eero Nikinmaa and Timo Vesala, "Modelling the SAR Response of Pine Forests in Southern Finland", Proceedings of IEEE International Geoscience and Remote Sensing Symposium (IGARSS03), Toulouse, France, Vol II, 1350-1352, July 2003.

[17] Williams M.L. and N Harris, "Demonstration of Reduced False Alarm Rates using Simulated L-Band Polarimetric SAR Imagery of Concealed Targets", Proceedings of the IEEE International Conference on Radar, pp535-540, Adelaide, Australia, September 2003.

[18] Dobson M.C., F T Ulaby, M Hallikainen and M El-Rayes, "Microwave Dielectric Behaviour of Wet Soil: Part II: Four-Component Dielectric Mixing Models", IEEE Transactions on Geoscience and Remote Sensing, vol. GRS-23, pp 35-46, 1985.

[19] Lang R.H., "Electromagnetic Scattering from a Sparse Distribution of Lossy Dielectric Scatterers", Radio Science, vol. 16, pp. 15-30, 1981.

[20] Lang R.H. and J S Sidhu, "Electromagnetic Scattering froma Layer of Vegetation: A Discrete Approach", IEEE Transactions on Geoscience and Remote Sensing, vol. 21, pp. 62-71, 1983

[21] Saatchi S.S., D M LeVine and R H Lang, "A Microwave Backscattering and Emmission Model for Grass Canopies", IEEE Transactions on Geoscience and Remote Sensing, vol. 32, #1, pp. 177-186, 1994.

[22] Williams M.L., S Quegan and D Blacknell, "Distribution of Backscattered Intensity in the Distyorted Born Approximation: Application to C-band SAR Images of Woodland", Waves in Random Media, vol. 7, pp. 643-660, 1997.

[23] Frisch U., "Wave Propagation in Random Media", in "Probabilistic Methods in Aplpied Mathematics", vol. 1, Ed. A T Bharrucha-Reid (New York: Academic), 1968.

[24] Ulaby F.T. and M A El-Rayes, "Microwave Dielectric Spectrum of Vegetation-PartII: Dual-Dispersion Model", IEEE Transactions on Geoscience and Remote Sensing, GE-25, pp 550-557, 1987.

[25] Carrara W.G. , R S Goodman and R M Majewski, "Spotlight Synthetic Aperture Radar Signal Processing Algorithms", Artech House (Boston, London), 1995.

[26] Karam M.A. and A K Fung, "Electromagnetic Scattering from A Layer of Finite, Randomly Oriented, Dielectric, Circular Cylinders Overa Rough Interface with Application to Vegetation", Radio Science, vol. 18, pp. 557-563, 1983.

[27] Williams M.L. and S Quegan, "Modelling Microwave Backscatter from Discrete Random Media using a Multiple-Scattering Series: Convergence Issues", Waves in Random Media, vol. 7, pp. 213-227, 1997.

[28] Schiffer R. and K O Thielheim, Journal of Applied Physics, vol. 50, pp. 2476-2483, 1979.

[29] Griesser T. and C A Balanis, "Backscatter Analysis of Dihedral Corner Reflectors using Physical Optics and the Physical Theory of Diffraction", IEEE Transactions on Antennas and Propagation, vol. AP-35, #10, pp 1137-1147, 1987.

[30] Ogilvy J.A. , "Theory of Scattering from Random Rough Surfaces", IOP Publishing, Bristol and Philadelphia, 1991.

[31] Luckman A.J. and J R Baker, "The Contribution of Trunk-Ground, Interactions to the SAR Backscatter from a Coniferous Forest", Proceedings of IEEE International Geoscience and Remote Sensing Symposium (IGARSS95), p2032, 1995.